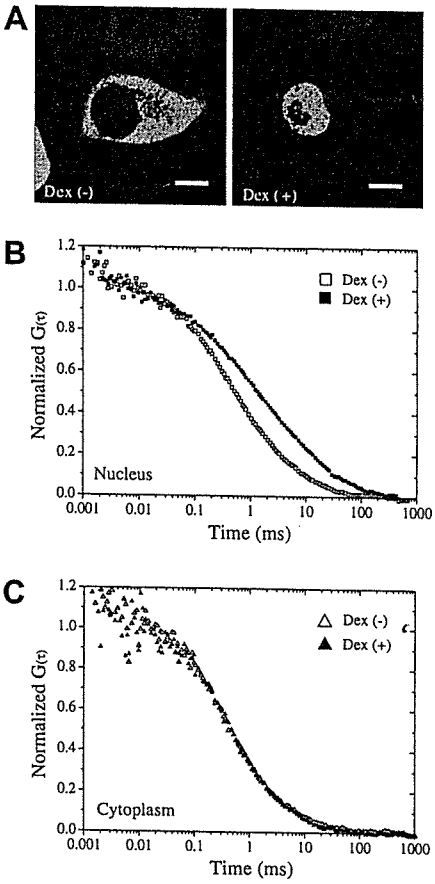

Fig. 2. LSM images and normalized FAFs in HeLa cells expressing EGFP-hGRα. (A) HeLa cells expressing EGFP-hGRα were imaged using confocal LSM, before (left) and 60 min after (right) addition of Dex to 100 nM. The scale bar represents 10 μm. FCS measurement performed (B) in the nuclei and (C) cytoplasm of HeLa cells expressing EGFP-hGRα, before (open squares) and 60 min after (closed squares) addition of Dex. The normalized FAFs were shifted to the right by addition of Dex at the nucleus.

3.3. The difference between mutants and the wild-type hGRα

To identify what part of hGRα changed the slow-moving diffusion in the presence of Dex, we constructed three mutants, as shown in Fig. 3.

As shown in Fig. 4A, B, C421G and A458T were translocated from the cytoplasm to the nucleus by exposure to Dex

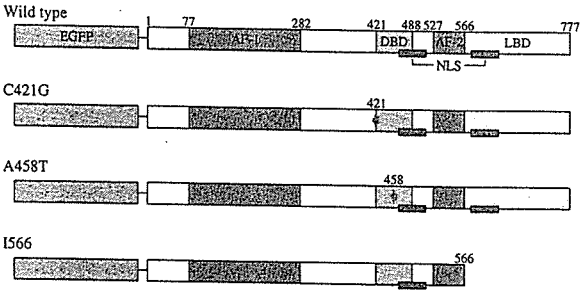

Fig. 3. Schematic structures of wild-type EGFP-hGRα and mutants. hGRα protein contains three major domains. The N-terminal transactivation domain consists of the activation function domain, which is required for transcriptional enhancement. The central DNA binding domain contains two zinc finger regions critical for receptor dimerization and target DNA binding. The C-terminal ligand binding domain serves as a binding site for coactivators, and contains nuclear localization signals. AF-1, activation function 1; DBD, DNA binding domain; AF-2, activation function 2; LBD, ligand binding domain; NLS, nuclear localization signal.

like the wild-type hGRα. Interestingly, there was no difference in the LSM images between the wild type and mutants; however, normalized FAFs of C421G and A458T (Fig. 5A, B) were different compared with the wild type of hGRα in the presence of Dex. Moreover, the effect of Dex on the shift of FAFs was in order of the wild type, A458T and C421G. On the other hand, the I566 mutant was localized in the nucleus independently of Dex stimulation, and normalized FAFs did not change (Fig. 6B). FAFs of mutants in the nuclei were analyzed by two-component fitting, and the average diffusion constants and fractions are summarized in Table 1. The first (fast moving) component of each mutant was not significantly affected by Dex. On the other hand, the diffusion constant of the second (slow moving) component decreased after addition of Dex (Fig. 7). Dex addition slowed the second components of A458T and C421G to 34.8% and 61.7% of those in the absence of Dex, respectively. A different diffusional property was observed in our experiment between A458T and C421G, although both mutants did not have transcriptional activity [11,12]. This result may indicate that slow-moving hGRα was affected by DNA binding rather than dimerization and could be an indicator of its transcriptional activity because A458T was more affected by Dex addition than C421G was. Moreover, although I566 localized in the nucleus, the diffusion con-

Table 1
Diffusion constants and fractions of wild-type hGRα and mutants in the nucleus

	Ligand	n	First		Second		
			DC1 (μm²/s)	F1 (%)	DC2 (μm²/s)	(Pdc (%))	F2 (%)
Wild type	Dex (−)	23	14.30 ± 4.87	60.7	1.60 ± 0.44		39.3
	Dex (+)	23	8.70 ± 2.59*	63.9	0.25 ± 0.09*	(15.6)	36.1
C421G	Dex (−)	25	15.08 ± 5.25	67.5	1.49 ± 0.48		32.5
	Dex (+)	23	13.71 ± 4.93	60.0	0.92 ± 0.36*	(61.7)	40.0
A458T	Dex (−)	23	16.54 ± 6.39	62.9	1.61 ± 0.64		37.1
	Dex (+)	24	12.96 ± 3.43	55.2	0.56 ± 0.11*	(34.8)	44.8
D566	Dex (−)	22	13.76 ± 2.46	59.4	1.07 ± 0.17		40.6
	Dex (+)	27	13.31 ± 2.56	62.9	0.96 ± 0.33	(60.0)[a]	37.1
Wild type	RU486 (+)	24	8.89 ± 3.93	64.8	0.86 ± 0.37*	(53.4)[a]	35.2

Diffusion constants (DC), fraction (F), number (n) of cells for FCS measurements in nucleus and percentage (Pdc) of diffusion constant in the absence (Dex (−)), to the presence of Dex (+) or RU486 (+).
*Significantly different ($P < 0.0001$).
[a]This value was compared with the wild type in the absence of Dex.

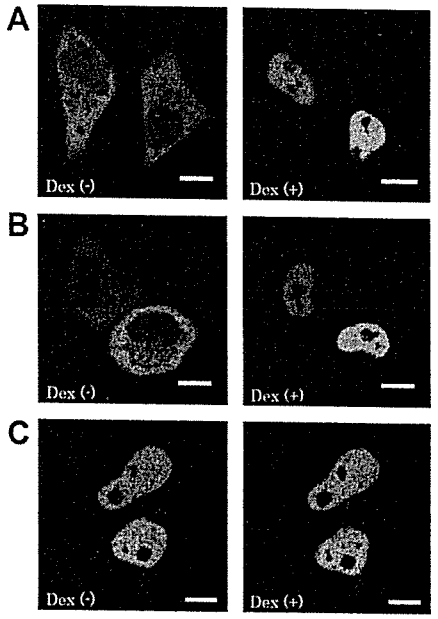

Fig. 4. Subcellular localization of EGFP-hGRα mutants. HeLa cells expressing (A) EGFP-hGRα/C421G, (B) EGFP-hGRα/A458T, (C) EGFP-hGRα/I566 were imaged before (left) and 60 min after (right) addition of Dex to 100 nM. The scale bar represents 10 μm. C421G and A458T were translocated to the nucleus by stimulation with Dex. I566 was localized in the nucleus before addition of Dex.

stant was only 60.0% of that of the wild type in the absence of Dex. This result also indicated that LBD had an important effect on slow-moving hGRα in the nucleus.

3.4. *The difference between the effects of agonists and antagonists on hGRα*

We also examined the effect of RU486, a transactivational antagonist of hGRα [16], in the nucleus. As shown in Fig. 6A, EGFP-hGRα was translocated to the nucleus by stimulation with RU486 as well as Dex. FAFs obtained in the nucleus before and after addition of RU486 (Fig. 6B) were analyzed by two-component fitting and the average diffusion constants and fractions are summarized in Table 1. It was confirmed that RU486 reduced the diffusion constant of wild type to 53.4% of that in the absence of Dex, although hGRα was translocated to the nucleus as well as with Dex (Fig. 2). This result demonstrated that agonist and antagonist were distinguished by diffusion analysis using FCS. The fast component of wild type in the presence of RU486 was also reduced. This result might relate to the result of wild type in the presence of Dex and may indicate that initial complex and/or unstable complex of GRα and cofactor in the presence of RU486 could be detected. However further study is needed to clarify this phenomena.

4. Conclusion

The activity of mutant hGRα in the nucleus can be determined according to differences of dynamic properties such as diffusion and translocation, which are obtained by FCS and LSM, respectively. However, our results suggested that the transactivation of hGRα was related more to the mobility of the protein than to its translocation from the cytoplasm to

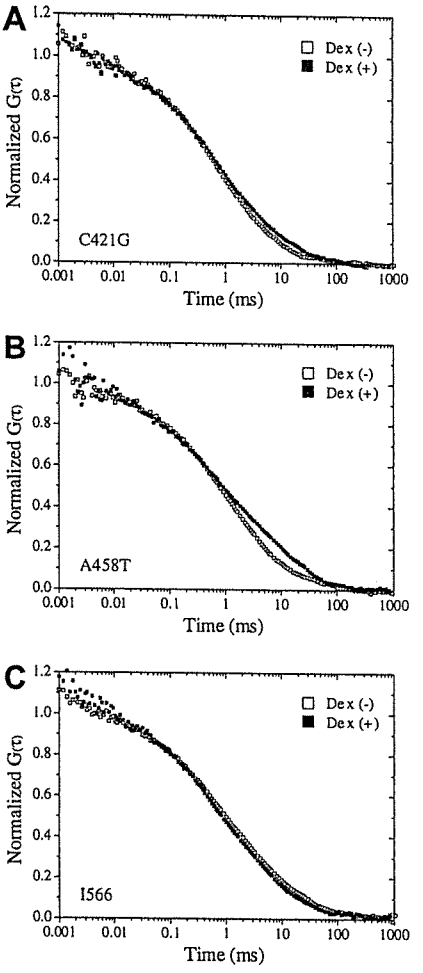

Fig. 5. Typical FAFs of EGFP-hGRα mutants in the nuclei before and after addition of Dex. FCS measurement performed in nuclei of HeLa cells expressing (A) EGFP-hGRα/C421G, (B) EGFP-hGRα/A458T, (C) EGFP-hGRα/I566 before (open squares) and 60 min after (closed squares) addition of Dex. All normalized FAFs differed from the wild type in the presence of Dex in the nucleus (see Fig. 2B).

the nucleus. We found that tethering of the diffusion was related to the transactivational process, such as DNA binding, dimerization and formation of complex of hGRα. Moreover, our results also suggested that dimerization of hGRα in the nucleus could act as a supportive factor to form the hGRα–GRE complex. Consequently, it is concluded that the biomolecule activity of hGRα with chemicals such as inhibitors, agonists and antagonists in cell compartments such as the nucleus can be determined through mobility analysis by FCS. However, the target binding site of GRα is mainly GRE in chromosomes; many associated proteins whose molecular size is not so large have also been identified in the cytoplasm. The interaction between such associated proteins and hGRα will be analyzed by advanced fluorescent techniques such as fluorescence cross-correlation spectroscopy (FCCS) since FCS can only detect large changes in molecular mass interactions such as chromosomes and hGRα. On the other hand, FCCS can detect protein–protein interactions in living cells when spectrally distinguishable fluorophores are available for each associated protein and GRα [17]. In this study, we confirmed that the combination of FCS and LSM is a feasible technique to clarify the highly dynamic mechanisms of biomolecules in living cells.

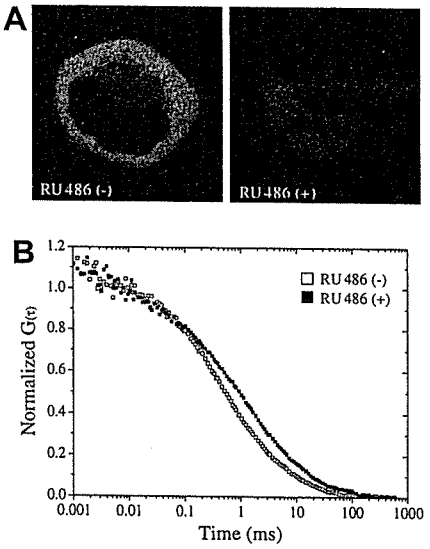

Fig. 6. The effect of RU486 on the localization and the mobility of EGFP-hGRα. (A) HeLa cells expressing EGFP-hGRα were imaged before (left) and 60 min after (right) addition of RU486 to 100 nM. The scale bar represents 10 μm. (B) FCS measurement performed in the nuclei of HeLa cells expressing EGFP-hGRα, before (open squares) and 60 min after (closed squares) addition of RU486. The normalized FAFs were smaller than with Dex (see Fig. 2B).

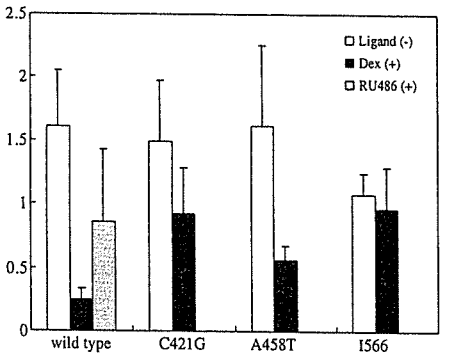

Fig. 7. Summary of the diffusion constants of second components. The white, black and gray bars indicate diffusion constants before addition of ligands, and after addition of Dex and RU486, respectively. After addition of Dex, the diffusion constants of the wild type, C421G and A458T decreased to 15.6%, 61.7%, and 34.8% of those in the absence of Dex, respectively. The diffusion constant of I566 decreased to 60.0% of that of the wild type in the absence of Dex. RU486 reduced the diffusion to 53.4% of that of the wild type in the absence.

Acknowledgments: This research was partly supported by Grands-in-Aid for Scientific Research (B) 15370062 and (A) 18207010 from the Japan Society for the Promotion of Science, and Grants-In-Aid for Scientific Research No. 16072201 in Priority Area "Molecular Nano Dynamics. (16072201)" and "Nuclear Dynamics (17050001)" by Ministry of Education, Culture, Sports, Science and Technology.

References

[1] Smoak, K.A. and Cidlowski, J.A. (2004) Mechanisms of glucocorticoid receptor signaling during inflammation. Mech. Ageing Dev. 125, 697–706.
[2] Schoneveld, O.J.L.M., Gaemers, I.C. and Lamers, W.H. (2004) Mechanisms of glucocorticoid signaling. Biochim. Biophys. Acta 1680, 114–128.
[3] Lu, N.Z. and Cidlowski, J.A. (2004) The origin and functions of multiple human glucocorticoid receptor isoforms. Ann. N.Y. Acad. Sci. 1024, 102–123.
[4] Schaaf, M.J.M. and Cidlowski, J.A. (2003) Molecular determinants of glucocorticoid receptor mobility in living cells: the importance of ligand affinity. Mol. Cell. Biol. 23, 1922–1934.
[5] Sprague, B.L., Pego, R.L., Stavreva, D.A. and McNally, J.G. (2004) Analysis of binding reactions by fluorescence recovery after photobleaching. Biophys. J. 86, 3473–3495.
[6] Kino, T., Liou, S.H., Charmandari, E. and Chrousos, G.P. (2004) Glucocorticoid receptor mutants demonstrate increased motility inside the nucleus of living cells: time of fluorescence recovery after photobleaching (FRAP) is an integrated measure of receptor function. Mol. Med. 10, 80–88.
[7] Lippincott-Schwartz, J., Snapp, E. and Kenworthy, A. (2001) Studying protein dynamics in living cells. Nat. Rev. Mol. Cell Bio. 2, 444–456.
[8] Saito, K., Ito, E., Takakuwa, Y., Tamura, M. and Kinjo, M. (2003) In situ observation of mobility and anchoring of PKCbetaI in plasma membrane. FEBS Lett. 541, 126–131.
[9] Kamada, A., Nagaya, H., Tamura, T., Kinjo, M., Jin, H.Y., Yamashita, T., Jimbow, K., Kanoh, H. and Wada, I. (2004) Regulation of immature protein dynamics in the endoplasmic reticulum. J. Biol. Chem. 279, 21533–21542.
[10] Pack, C., Saito, K., Tamura, M. and Kinjo, M. (2006) Microenvironment and effect of energy depletion in the nucleus analyzed by mobility of multiple oligomeric EGFPs. Biophys. J. 91, 3921–3936.
[11] Ray, A., LaForge, K.S. and Sehgal, P.B. (1991) Repressor to activator switch by mutations in the first Zn finger of the glucocorticoid receptor: is direct DNA binding necessary? Proc. Natl. Acad. Sci. USA 88, 7086–7090.
[12] Adams, M., Meijer, O.C., Wang, J., Bhargava, A. and Pearce, D. (2003) Homodimerization of the glucocorticoid receptor is not essential for response element binding: activation of the phenylethanolamine *N*-methyltransferase gene by dimerization-defective mutants. Mol. Endocrinol. 17, 2583–2592.
[13] Okamoto, K., Tanaka, H., Ogawa, H., Makino, Y., Eguchi, H., Hayashi, S., Yoshikawa, N., Poellinger, L., Umesono, K. and Makino, I. (1999) Redox-dependent regulation of nuclear import of the glucocorticoid receptor. J. Biol. Chem. 274, 10363–10371.
[14] Nomura, Y., Tanaka, H., Poellinger, L., Higashino, F. and Kinjo, M. (2001) Monitoring of in vitro and in vivo translation of green fluorescent protein and its fusion proteins by fluorescence correlation spectroscopy. Cytometry 44, 1–6.
[15] Chen, J., Blackford Jr., J.A. and Simons Jr., S.S. (2004) PCR expression mutagenesis: a high-throughput mutation assay applied to the glucocorticoid receptor ligand-binding domain. Biochem. Biophys. Res. Co. 321, 893–899.
[16] Cadepond, F., Ulmann, A. and Baulieu, E.-E. (1997) RU486 (MIFEPRISTONE): mechanisms of action and clinical uses. Annu. Rev. Med. 48, 129–156.
[17] Kogure, T., Karasawa, S., Araki, T., Saito, K., Kinjo, M. and Miyawaki, A. (2006) A fluorescent variant of a protein from the stony coral Montipora facilitates dual-color single-laser fluorescence cross-correlation spectroscopy. Nat. Biotechnol. 24, 577–581.

Published online 16 August 2006

Nucleic Acids Research, 2006, Vol. 34, No. 14 **e102**
doi:10.1093/nar/gkl477

Protein–protein interaction analysis by C-terminally specific fluorescence labeling and fluorescence cross-correlation spectroscopy

Rieko Oyama, Hideaki Takashima, Masato Yonezawa, Nobuhide Doi, Etsuko Miyamoto-Sato, Masataka Kinjo[1] and Hiroshi Yanagawa*

Department of Biosciences and Informatics, Keio University, Yokohama 223-8522, Japan and [1]Research Institute for Electronic Science, Hokkaido University, Sapporo 060-0812, Japan

Received May 22, 2006; Revised and Accepted June 20, 2006

ABSTRACT

Here, we describe novel puromycin derivatives conjugated with iminobiotin and a fluorescent dye that can be linked covalently to the C-terminus of full-length proteins during cell-free translation. The iminobiotin-labeled proteins can be highly purified by affinity purification with streptavidin beads. We confirmed that the purified fluorescence-labeled proteins are useful for quantitative protein–protein interaction analysis based on fluorescence cross-correlation spectroscopy (FCCS). The apparent dissociation constants of model protein pairs such as proto-oncogenes c-Fos/c-Jun and archetypes of the family of Ca^{2+}-modulated calmodulin/related binding proteins were in accordance with the reported values. Further, detailed analysis of the interactions of the components of polycomb group complex, Bmi1, M33, Ring1A and RYBP, was successfully conducted by means of interaction assay for all combinatorial pairs. The results indicate that FCCS analysis with puromycin-based labeling and purification of proteins is effective and convenient for *in vitro* protein–protein interaction assay, and the method should contribute to a better understanding of protein functions by using the resource of available nucleotide sequences.

INTRODUCTION

An understanding of the rate and specificity of assembly of biomolecular complexes is essential for a full appreciation of the mechanisms of biological events. Further, currently available information on genome sequences of various organisms can be exploited as a resource for characterizing novel functions of proteins or hypothetical proteins. For this purpose, a high-throughput method is required for functional protein analysis. Fluorescence correlation spectroscopy (FCS) and fluorescence cross-correlation spectroscopy (FCCS) have recently been applied to such important biological problems (1–11). FCS allows monitoring of the individual movements of fluorescence-labeled molecules through a very tiny area (1,2). The time-dependent fluorescence autocorrelation function allows us to analyze the relative proportions of species involved in the diffusion. Changes of the proportions can be used to calculate the binding kinetics (3,4,8). FCCS utilizes separate channels to detect two distinct fluorophores, as well as the cross-correlated signals, in real time (5). With FCCS, bound molecules can be detected even if the differences of diffusion are not great. So far, FCCS has been applied to the studies of DNA hybridization (5), PCR (9), enzymatic cleavage of a DNA substrate by EcoRI endonuclease (6,10) and protein–DNA interactions (11).

Fluorescence labeling of proteins is a key step for the FCS and FCCS analysis of protein interactions. So far, chemical modifications (12,13) and recombinant fusion tagging with fluorescent proteins (14–17) have been used for fluorescence labeling of proteins. These methods are often useful, but the modifications of internal amino acid residues or the addition of relatively large fluorescent proteins may affect the functions of labeled proteins. As an alternative approach, we have previously developed a puromycin-based method for fluorescence labeling of proteins (18,19). By using this method, various fluorophores can be incorporated into full-length proteins in the presence of a low concentration of fluorophore-conjugated puromycin in a cell-free translation system (11). Small fluorescent probes are expected to be less likely to interfere with the structure or biological function of proteins and cell-free protein synthesis is suitable for a high-throughput format owing to its simplicity. We have previously reported the FCCS analysis of protein–DNA

*To whom correspondence should be addressed. Tel: +81 45 566 1775; Fax: +81 45 566 1440; Email: hyana@bio.keio.ac.jp
Present addresses:
Rieko Oyama, RIKEN, Genome Science Laboratory, 2-1 Hirosawa, Wako 351-0198, Japan
Masato Yonezawa, Research Institute of Molecular Pathology (IMP), Vienna, Austria

interactions between RhG (rhodamine green)-labeled proteins and Cy5-labeled DNA (11). Although high-throughput analysis of protein–protein interactions in solution using FCCS is of great interest, detection of cross-correlations between differently labeled proteins has been difficult, because the labeling efficiency of our method ranges from only 10 to 30% (11), and the remaining unlabeled proteins in solution inhibit the formation of the protein–protein complex carrying both RhG and Cy5. In this study, we have improved the purification process of fluorescence-labeled proteins by using novel iminobiotin-conjugated fluorescent puromycin derivatives to aid the removal of unlabeled proteins, thereby making protein–protein interaction assay using FCCS practically feasible. We used three model systems, proto-oncogenes c-Fos and c-Jun, archetypes of the family of Ca^{2+}-modulated calmodulin (CaM) and CaM-related binding proteins, and the polycomb group (PcG) complex proteins to confirm the usefulness of our method.

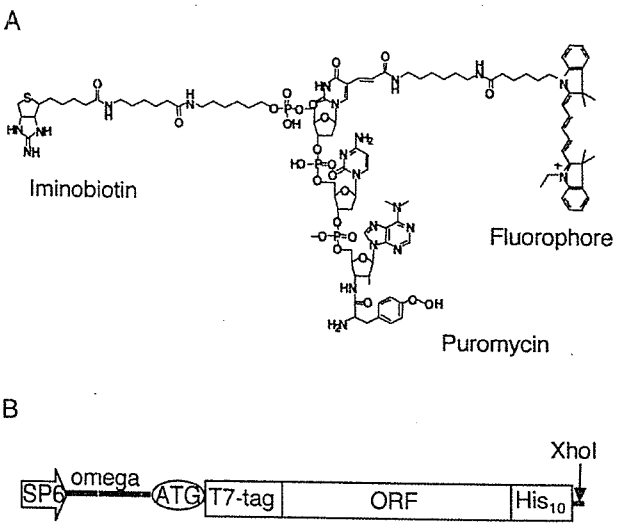

Figure 1. Materials for fluorescence labeling. (A) The structure of a fluorescent puromycin derivative. A fluorophore (Cy5 or RhG) and iminobiotin were chemically conjugated to puromycin through a linker. (B) DNA construction for fluorescence labeling of proteins. Template DNA consists of SP6 promoter, Omega sequence and an open reading frame (ORF) with a T7-tag at the N-terminus and a polyhistidine tag at the C-terminus, followed by a XhoI restriction enzyme site.

MATERIALS AND METHODS

Synthesis of fluorescent puromycin derivatives

NHS-iminobiotin trifluoroacetamide was purchased from Pierce. Iminobiotin-T(Cy5)-dC-puromycin (Figure 1A) and iminobiotin-T(RhG)-dC-puromycin (data not shown) were synthesized and purified as described previously (11), with some modifications (see Supplementary Data). The structural identity of the synthesized fluorescent puromycin analogs was confirmed by MALDI-TOF mass spectrometry (Voyager; Perceptive Biosystems).

Preparation of templates for translation

In a template DNA, two tags were added to the 5′- and 3′-termini of the open reading frame (11,19) (Figure 1B) by PCR and the fragment was subcloned into a pCR2.1Topo vector (Invitrogen). The DNA template was amplified from the clone by PCR and cleaved with XhoI. The purified DNA was transcribed in an SP6 large-scale RNA production system (Promega).

Fluorescence labeling and purification

Fluorescence labeling was carried out using the wheat germ extract translation system 'Proteios' (Toyobo, Japan) as described in the manufacturer's protocol, except that a fluorophore-conjugated puromycin was added. The translation was terminated by the addition of RNase A (1 μg/0.3 ml; Ambion). The purification of fluorescently labeled proteins was performed at 4°C. The mixture was dialyzed against nickel binding buffer (50 mM phosphate, 150 mM NaCl, 1 mM DTT and 0.05% NP-40, pH 8.0), followed by centrifugation at 16 000 *g* for 20 min. The supernatant was mixed with 10 μl of Ni-NTA agarose (20) (SuperFlow; Qiagen) for 1 h. The supernatant was removed, and the beads were washed three times, with agitation, in nickel binding buffer (1.0 ml) containing 2.5 mM imidazole and 300 mM NaCl. Proteins were eluted with 50 μl of buffer containing 0.5 M imidazole, pH 8.0. The fraction was mixed with 9 vol of 50 mM phosphate buffer (pH 8.0) containing 300 mM NaCl, 5 mM DTT and 0.05% NP-40, then 10 μl of streptavidin–Sepharose (21) (Amersham Pharmacia) was added and the mixture was rocked for 1 h. The beads were washed with the buffer three times. Protein was eluted with 50 μl of buffer (240 mM Tris–HCl, 150 mM NaCl, 0.1 M biotin, 5 mM DTT and 0.1% NP-40, pH 8.0). The protein fraction was mixed with 10 mM DTT and kept at 4°C before use.

Immunodetection and fluorescence determination

The proteins were detected by enhanced immunoblotting (22) with mouse anti-T7-tag antibody (Novagen) and horseradish peroxidase (HRP)-labeled goat anti-mouse IgG (Transduction Laboratories). The blot was determined semiquantitatively with the T7-tag positive control recombinant protein (Novagen), an ECL detection kit (Amersham Pharmacia) and a CCD camera (ChemiDoc; Bio-Rad). Proteins separated by SDS–PAGE were stained with SyproOrange (Molecular Probes) and detected using a fluorescence image analyzer (excitation at 488 nm and emission at 515–545 nm, Molecular Imager FX; Bio-Rad). The fluorescence yield was spectrophotometrically determined using the fluorescence image analyzer (Cy5 was detected with excitation at 635 nm and emission at 670–720 nm; RhG with excitation at 488 nm and emission at 515–545 nm) and a standard dye with molecular extinction coefficients of ε_{505} (RhG) = 68 000 cm^{-1} M^{-1} (measured at pH 8.0) and ε_{647} (Cy5) = 250 000 cm^{-1} M^{-1}.

FCCS measurement

FCCS measurement was performed on a ConfoCor2 system (Carl Zeiss) as described previously (11). The two pinholes and the cross-correlated volume element were adjusted by

measurement (5). All solutions were prepared in water (fluorescence analysis grade; Dojindo, Japan) and filtered through an Ultrafree-MC filter unit (Millipore). Fluorescently labeled proteins were dialyzed against 50 mM phosphate, 150 mM NaCl, 0.1% NP-40 and 1 mM DTT, pH 7.4. After centrifugation at 16 000 *g* for 20 min, differently labeled proteins were mixed in a Lab-Tek 8-well chamber (Nalge Nunc) and kept for 10 min. Interaction of c-Fos with c-Jun was also analyzed in the presence of DNA, poly(dI–dC)·poly(dI–dC) (2 μg/ml; Amersham Pharmacia) and the AP-1 synthetic oligonucleotides of 30 bp (Dateconcept, Sapporo, Japan) (23). CaM interactions were analyzed in the presence of 0.5 mM $CaCl_2$. Two autocorrelation curves and the cross-correlation curve of FCCS data were analyzed by using fitting algorithm described below in the software package for ConfoCor2 (Carl Zeiss).

Theory and data calibration

The theoretical background of FCCS analysis has been described by Eigen *et al.* and Rigler *et al.* (5,6,9). The fluorescence autocorrelation function and the cross-correlation function were acquired from an online system-controlling computer software package. The normalized cross-correlation function $G(\tau)$ is given by

$$G_{gr}(\tau) = 1 + \frac{\langle \delta I_g(t) \cdot \delta I_r(t+\tau) \rangle}{\langle I_g \rangle \cdot \langle I_r \rangle}, \quad 1$$

where the indices refer to one or two measured fluorescence signals, I_g and/or I_r. In the case of one fluorescent species, Equation 1 (r = g) defines normalized autocorrelation function in a single detection channel. ω_1 is the radius and ω_2 is half of the long axis of the confocal volume element. The structural parameter S is the ratio of ω_2/ω_1. Two-component model of the autocorrelation function for translational diffusion in a 3D Gaussian volume element is described as follows:

$$G(\tau) = 1 + \frac{1}{N} \cdot \left[(1-Y) \cdot \left(1 + \frac{\tau}{\tau_{D_1}}\right)^{-1} \cdot \left(1 + \frac{\tau}{S^2 \tau_{D_1}}\right)^{-1/2} + Y \cdot \left(1 + \frac{\tau}{\tau_{D_2}}\right)^{-1} \cdot \left(1 + \frac{\tau}{S^2 \tau_{D_2}}\right)^{-1/2} \right], \quad 2$$

where τ_{D_1} and τ_{D_2} are the diffusion times of the faster component and slower component in the assay. Y represents the fraction of fluorescent protein with the diffusion time τ_{D_2} in the total number of fluorescent particles N. The values of $\omega_{1,i}$ (i = g or r) were determined from the diffusion times of rhodamine 6G (Sigma Aldrich; diffusion coefficient $D = 2.8 \times 10^{-10}$ m^2 s^{-1}) and Cy5 (mono-reactive dye, Amersham Pharmacia; $D = 3.16 \times 10^{-10}$ m^2 s^{-1}).

$$\omega_{1,i} = \sqrt{4D \cdot \tau_{D_i}} \quad 3$$

The volume elements V are calculated according to

$$V_i = \pi^{3/2} \cdot \omega_{1,i}^2 \cdot \omega_{2,i} \quad 4$$

$$V_{gr} = \left(\frac{\pi}{2}\right)^{3/2} (\omega_{1,g}^2 + \omega_{1,r}^2)(\omega_{2,g}^2 + \omega_{2,r}^2)^{1/2} \quad 5$$

The measured total number of autocorrelated particles $N_{AC,i}$ and complex cross-correlated particles N_{cc} is given by

$$N = \frac{1}{G_i(0) - 1} \quad 6$$

where in the case of N_{cc}, $G_i(0)$ indicates $G_{gr}(0)$. The red emission excited by the green laser Q_g (cross-talk fraction) was calculated from the mean count rates of the red channel when excited by both lasers (C_{gr}) and only the red laser (C_r), using a modification of the method in the application manual of ConfoCor2.

$$Q_g = \frac{C_{gr} - C_r}{C_{gr}} \quad 7$$

Calculated free molecules N_i and calculated complex molecules N_{gr} are as follows:

$$N_{AC,g} = N_g + N_{gr} \quad 8$$

$$N_{AC,r} = N_r + Q_g \cdot N_g + (1 + Q_g) \cdot N_{gr} \quad 9$$

$$N_{gr} = \frac{N_{AC,g} \cdot (N_{AC,r} + Q_g \cdot N_{AC,g})}{N_{cc} - Q_g \cdot N_{AC,g}}. \quad 10$$

The concentrations of each fluorescent protein were calculated with the use of A (Avogadro's number) as follows:

$$c_i = \frac{N_i \cdot Y_i}{V_i \cdot A}. \quad 11$$

The dissociation constants (K_ds) are given by

$$K_d = \frac{(c_r - c_{gr}) \cdot (c_g - c_{gr})}{c_{gr}}. \quad 12$$

RESULTS

Tandem affinity purification of fluorescently labeled proteins

c-Fos(118–211) and c-Jun(216–318) were translated in the presence of iminobiotin–fluorophore-conjugated puromycin, whose structure is presented in Figure 1A. The optimal concentrations of the puromycin derivatives were 12.5 μM as RhG and 25 μM as Cy5, respectively (data not shown). The reaction mixtures were purified by two steps of affinity purification with nickel-chelate beads (Figure 2A) and streptavidin-conjugated beads (Figure 2B). Excess unincorporated dyes and lower molecular weight proteins were not retained on nickel-chelate beads (Figure 2A, lane 2). The fractions eluted with 0.5 M imidazole (Figure 2A, lane 3) were further purified using streptavidin beads. The flow-through fraction contained <5% of the total fluorescence intensity, but ~30% of the immunoblotting signal (Figure 2B, lane 2). The biotin-eluted fraction (Figure 2B, lane 3) showed a weaker signal than that of the applied fraction (Figure 2B, lane 1) in immunodetection. These results indicate that unlabeled proteins were successfully removed by the second step of affinity purification. The

purified Cy5–protein fraction was identical to one band detected in SDS–PAGE by protein staining with SyproOrange (Figure 2C, lane 2). Similarly, CaM, CaM-binding proteins and PcG proteins were labeled and highly purified (data not shown).

Conditions of FCCS analysis with ConfoCor2

The pinhole diameters were adjusted to 70 μm in the green channel and 48 μm in the red channel to provide a sufficient observation volume for our system. The overlap of the excitation volumes between red and green laser lines was achieved by exciting the Cy5 dye with both wavelengths (5). The autocorrelation curve of the red channel with only the 633 nm laser (red line in Supplementary Figure 1) was coincident with the curve of the channel with only the 488 nm laser (blue line in Supplementary Figure 1). The particle numbers detected in the red channel and in the green channel were 24.1 and 23.7, respectively. The structural parameter S was calculated as 5 for the green channel and as 7 for the red channel. The diffusion time of ~10 nM rhodamine 6G in the green channel was 30 μs and that of ~10 nM Cy5 dye in the red channel was 44 μs in the laser power range used. The effective volume elements were V_g = ~0.19 fl in the green channel, V_r = ~0.41 fl in the red channel and V_{gr} = ~0.26 fl in the cross-correlated channel (see Equations 4 and 5 in Materials and Methods for definitions). The differences between these detection volumes were accounted for in the data analysis according to Equation 11. The calculated diffusion coefficients of iminobiotin-T(RhG)-dC-puromycin and iminobiotin-T(Cy5)-dC-puromycin were 2.1 and 2.3 × 10^{-10} m^2 s^{-1}, respectively, using FCS analysis. The cross-talk from red to green was zero whereas the cross-talk from green to red was ~10%: this was accounted for in the calculation of complex concentration according to Equation 10.

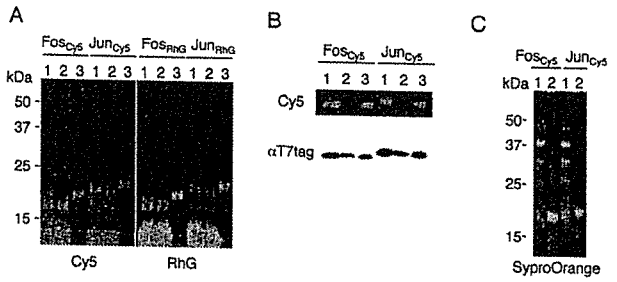

Figure 2. Purification of fluorescence-labeled proteins. Subscript Cy5 or RhG indicates a fluorophore linked to puromycin derivative. Proteins were separated on 15–25% continuous gradient SDS–PAGE and detected using a fluorescence imager (Cy5 or RhG) or αT7-tag antibody. (A) Affinity purification with nickel-chelate resin. Lane 1, *in vitro* translation products; lane 2, flow-through fractions; and lane 3, eluates with 0.5 M imidazole. (B) Affinity purification with streptavidin resin. Lane 1, nickel-chelate affinity-purified fractions; lane 2, flow-through; and lane 3, eluates with 0.1 M biotin. (C) Protein staining with SyproOrange. Lane 1, *in vitro* translation products; and lane 2, purified fractions.

FCCS analysis of c-Fos and c-Jun

The fractions of fluorescently labeled proteins to fluorescent particles were c-Fos_{Cy5} 71%, c-Jun_{Cy5} 68%, c-Fos_{RhG} 69% and c-Jun_{RhG} 67% when the functions were fitted to two-component models with diffusion times corresponding to those of the fluorescent derivatives using FCS analysis (Figure 3). Diffusion coefficients of c-Fos_{RhG}, c-Fos_{Cy5}, c-Jun_{RhG} and c-Jun_{Cy5} were calculated to be 7.6–8.1 × 10^{-11} m^2 s^{-1}. As shown in Supplementary Figure 2, the diffusion coefficients of fluorescent-puromycin-labeled proteins were consistent with the predictions of the Stokes–Einstein theory (24). Concentrations of fluorescently labeled proteins were calculated from the autocorrelation functions in the FCCS analysis (Figure 3A–C, upper panels). The apparent K_d values calculated with the equilibrium data are summarized in Table 1. The translational diffusion time of c-Fos

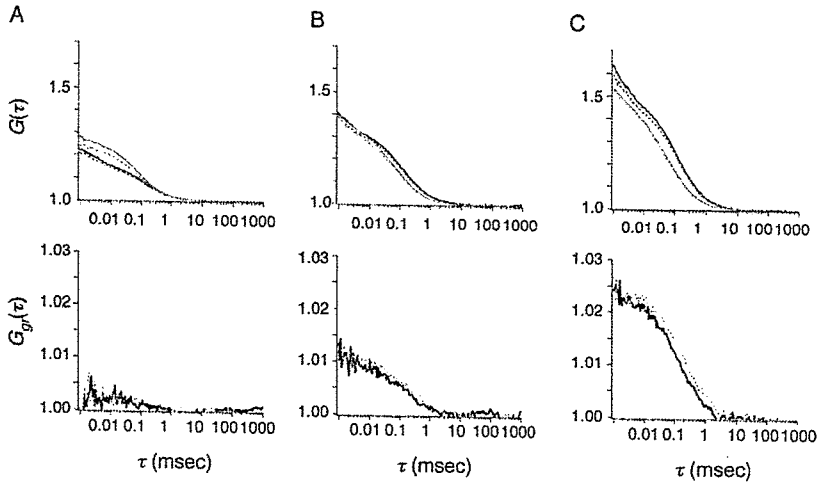

Figure 3. FCCS analysis of AP-1-binding proteins. The autocorrelation function (upper panels) and cross-correlation function (lower panels) of c-Fos_{Cy5} and c-Fos_{RhG} (A), c-Jun_{Cy5} and c-Jun_{RhG} (B), and c-Jun_{Cy5} and c-Fos_{RhG} (C). In the autocorrelation plot, red and green lines represent Cy5 and RhG. The dashed curves (blue in cross-correlation function) represent data obtained after the addition of 50 nM AP-1 oligonucleotides.

homodimer was determined after the addition of AP-1 DNA by using the cross-correlation function (Figure 3A, lower panel). In the presence of the AP-1 DNA sequence, the K_d of the heterodimer was ~80-fold lower than that of c-Fos homodimer (Table 1). In the case of the heterodimer and c-Jun homodimer, the K_d decreased to ~70% after the addition of the AP-1 sequence. The cross-correlation function of c-Fos_{RhG}/c-Jun_{Cy5} gave the diffusion coefficient of the cross-correlated complex as 7.0×10^{-11} m^2 s^{-1} in the absence of the AP-1 sequence and 4.4×10^{-11} m^2 s^{-1} in its presence (Figure 3C, lower panel). The K_d of c-Fos_{Cy5}/c-Jun_{RhG} was determined to be 7×10^{-8} M in the absence of the AP-1 sequence and 5×10^{-8} M in its presence (data not shown).

FCCS analysis of CaM and CaM-binding proteins

The diffusion coefficients of $CaM(1–149)_{RhG}$, calcineurin $A(328–521)_{Cy5}$, $Rab3A(1–219)_{Cy5}$ and $caldesmon(302–564)_{Cy5}$ were calculated to be 7.6, 7.3, 6.8 and 7.0×10^{-11} m^2 s^{-1}, respectively. Variations of the cross-correlation function between CaM and CaM-binding proteins were observed in the presence of Ca^{2+} (see Figure 4A–C, solid curves). The diffusion times of the cross-correlated functions were determined, except for that of Rab3A, by using analyzing software. The amplitudes of the cross-correlation functions were reduced by the addition of EGTA (Figure 4B and C, dashed blue curves), indicating the involvement of Ca^{2+}-mediated interactions. The calculated K_ds after the addition of EGTA indicated a non-specific-binding interaction or the background of the detection procedure. The significant K_d values were determined to be $2–5 \times 10^{-7}$ M in the assay (Table 1).

Table 1. Concentrations of fluorescent proteins and apparent K_d values determined using FCCS in this study

Cy5-labeled protein (nM)	RhG-labeled protein (nM)	Addition	K_d (nM)
Fos (18.4)	Fos (18.0)	—	ND
Fos (19.2)	Fos (17.9)	AP-1 DNA	3720
Jun (8.1)	Jun (15.2)	—	270
Jun (7.8)	Jun (14.6)	AP-1 DNA	190
Jun (4.8)	Fos (12.3)	—	69
Jun (4.5)	Fos (11.5)	AP-1 DNA	45
Rab3A (4.8)	CaM (8.1)	—	ND
Rab3A (4.5)	CaM (7.8)	EGTA	ND
Caldesmon (6.1)	CaM (8.3)	—	500
Caldesmon (5.7)	CaM (7.5)	EGTA	2300
Calcineurin (11.2)	CaM (7.8)	—	160
Calcineurin (11.5)	CaM (7.9)	EGTA	2200
M33 (5.6)	Bmi1 (7.8)	—	92
M33 (4.6)	RYBP (5.3)	—	70
M33 (5.2)	Ring1A (7.7)	—	51
Ring1A (4.6)	RYBP (16.3)	—	74
Bmi1 (4.4)	RYBP (14.7)	—	2300
Bmi1 (4.1)	Ring1A (5.5)	—	2000

ND; not determined.

FCCS analysis of PcG complex proteins

The diffusion coefficients of fluorescently labeled proteins $M33(1–519)_{Cy5}$, $Bmi1(1–326)_{Cy5}$, $Bmi1(1–326)_{RhG}$, $Ring1A(201–377)_{Cy5}$, $Ring1A(201–377)_{RhG}$, $RYBP(92–228)_{Cy5}$ and $RYBP(92–228)_{RhG}$ were 4.1, 6.1, 6.6, 7.2, 7.4, 7.3 and 7.5×10^{-11} m^2 s^{-1}, respectively. Variations of cross-correlation function were observed for $Bmi1_{RhG}$/$M33_{Cy5}$, $M33_{Cy5}$/$Ring1A_{RhG}$, $M33_{Cy5}$/$RYBP_{RhG}$ and $RYBP_{RhG}$/$Ring1A_{Cy5}$ (solid curves shown in Figure 5A–D and Table 1). The significant interactions are shown schematically in Figure 6. M33 appeared to mediate the association. To confirm the role of M33, we examined the association with the mediator using FCCS. Interestingly, the amplitude of the cross-correlation function of $Bmi1_{Cy5}$/$Ring1A_{RhG}$ was increased by the addition of non-labeled M33 (dashed blue curves shown in Figure 5F). The diffusion coefficient of the cross-correlated complex was 2.7×10^{-11} m^2 s^{-1}, corresponding to ~120 kDa. The molecular brightness (C/M) was not altered by the addition of a non-labeled protein (19.5–20.0 kHz in the red channel and 12.7–11.3 kHz in the green channel). In contrast, the effect of the addition of M33 on the interactions of Ring1A/RYBP and Bmi1/RYBP was not significant (dashed blue curves in Figure 5D and E).

DISCUSSION

Purification of fluorescently labeled proteins by using a secondary affinity tag, iminobiotin, introduced on to fluorescent puromycin as described here, improved the sensitivity for FCCS analysis of interactions between two distinct fluorescence-labeled proteins. Indeed, the c-Jun_{RhG}/c-Jun_{Cy5} interactions both with and without non-labeled AP-1 oligonucleotide could be detected in this study, whereas the interaction among c-Jun_{RhG}/Cy5-labeled AP-1/non-labeled Jun

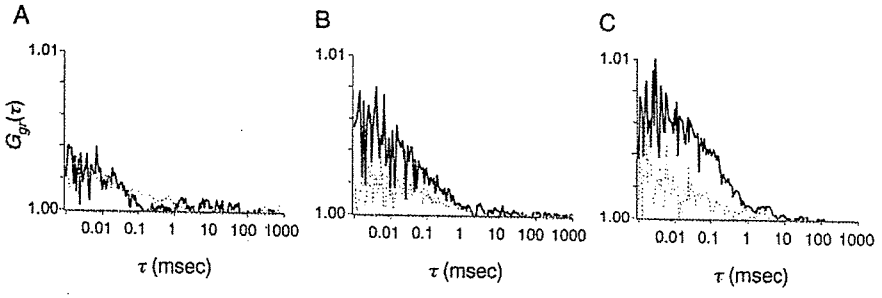

Figure 4. Cross-correlation function between CaM_{RhG} and CaM-binding proteins: $Rab3A_{Cy5}$ (A), $caldesmon_{Cy5}$ (B) and calcineurin $A\alpha_{Cy5}$ (C). The dashed blue curves represent data obtained after the addition of 5 mM EGTA.

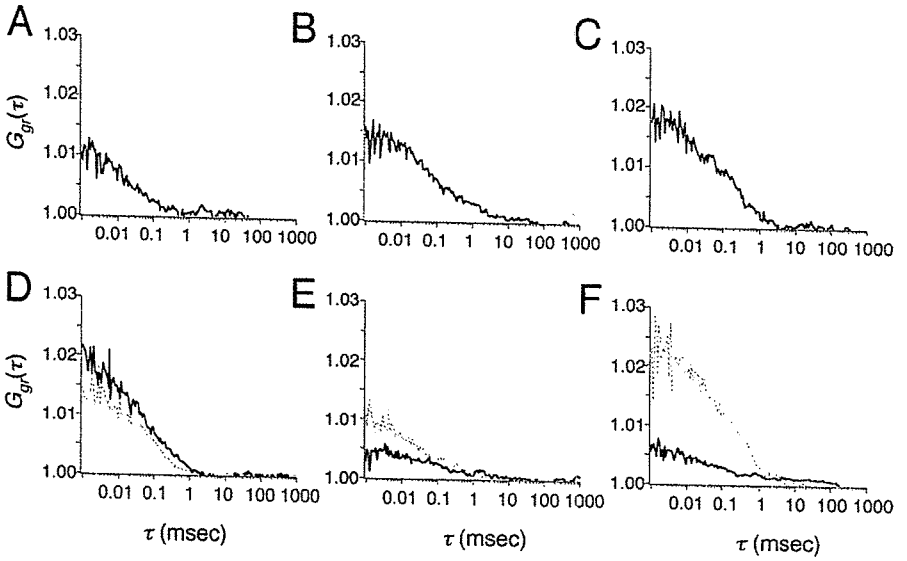

Figure 5. Cross-correlation function of $M33_{Cy5}$ and $Bmi1_{RhG}$ (**A**), $M33_{Cy5}$ and $Ring1A_{RhG}$ (**B**), $M33_{Cy5}$ and $RYBP_{RhG}$ (**C**), $Ring1A_{Cy5}$ and $RYBP_{RhG}$ (**D**), $Bmi1_{Cy5}$ and $RYBP_{RhG}$ (**E**), and $Bmi1_{RhG}$ and $Ring1A_{Cy5}$ (**F**). Dashed blue curves represent data obtained after the addition of non-labeled M33 (2 nM).

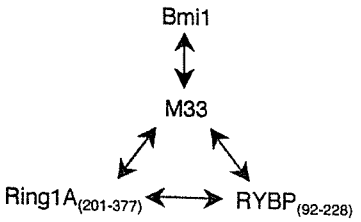

Figure 6. Schematic diagram of association of polycomb gene complex proteins. Arrows indicate interactions between the proteins as judged from the apparent K_d values in this study. Gray areas indicate triplet interaction detected using FCCS.

was not detected in the previous study (11). The apparent K_d of c-Fos/c-Jun/AP-1 found in this study was in good agreement with reported values (25,26). The K_d of c-Jun homodimer and AP-1 sequence also coincided with the value of 140 nM determined previously (25). Further, the K_d of CaM and caldesmon was in agreement with the reported value of 550 nM (27). The apparent K_d was independent of the concentrations of fluorescence-labeled proteins (data not shown). These results indicate that FCCS analysis with puromycin-based labeling of proteins is effective and convenient for protein–protein interaction assay, and that the puromycin derivatives and affinity tags did not interfere substantially with the protein interactions. It should be noted that the K_d values obtained from FCCS are minimum estimates because small amounts of unlabeled proteins may remain.

The interaction of c-Fos homodimer and CaM/Rab3A mediated by Ca^{2+} could not be identified in this study. The K_d of c-Fos homodimer and AP-1 sequence was previously reported to be ~6 μM (28). The K_d of CaM/Rab3A was also reported to be 20–50 μM (29,30). The interaction of c-Fos homodimer (and c-Jun homodimer) in this study might include interactions between single-colored proteins, but the molecular brightness was not greater than that of other probed proteins (data not shown). Such weak interactions might be detected if the concentrations of fluorescently labeled proteins were increased.

A surface plasmon resonance (SPR) biosensor allows real-time analysis of specific interactions on a solid phase, whereas FCS and FCCS detect interactions in solution. Schubert *et al.* (31) compared the entropic contribution to the free energy between SPR and FCS and concluded that the reaction entropy determined from an SPR experiment was lower than that from an FCS experiment. Indeed, the K_d between CaM and calcineurin was determined as 1.7×10^{-8} M by means of an SPR biosensor (32), and this is 10 times lower than our value using FCCS. Similarly, interaction assay of c-Fos/c-Jun heterodimer immobilized on a polystyrene tray gave a K_d of 1 nM (33), whereas our FCCS analysis gave 70 nM. Although the immobilizing method may be advantageous for the detection of protein interactions with low affinity, we believe that K_d values in living cells are likely to be more similar to those determined using FCCS in solution than to those determined on a solid phase.

The PcG proteins form multimeric complexes that bind to specific genomic sites of polycomb repressive elements (34). We applied FCCS to analyze in detail the individual associations of some PcG proteins by interaction assay of the pairs under homogeneous conditions. As shown in Table 1, significant interactions were found among M33/Bmi1, M33/Ring1A, M33/RYBP and Ring1A/RYBP, respectively, as previously confirmed by the yeast two-hybrid method and protein pulldown assay (35,36). It appears that M33 is a mediator in the association of these proteins (Figure 6), but only the association of Bmi1/M33/Ring1A was confirmed (Figure 5F). The association of Bmi1/M33/Ring1A was also supported by applying a three-component model to fit the autocorrelation function of Bmi1 after the addition of non-labeled M33 (data not shown). Bmi1, M33 and Ring1A are components of a stable core PcG repressive complex, according to a biochemical study (37). Interestingly, our

results suggest that RYBP may interact with M33 or Ring1A in the free form without the formation of a core complex. This is consistent with the idea that RYBP plays a role in recruiting PcG components (38). The FCCS analysis of the components of PcG complex proteins presented here should be a good model for detailed analysis of other protein complexes. For example, use of puromycin-based fluorescently labeled proteins would allow FCCS analysis, as well as FCS analysis, of the dynamics of complex formation of retinoblastoma tumor suppressor complex (39). The range of detectable interactions should be improved by using FCCS.

The tandem affinity purification method using a polyhistidine tag and an iminobiotin tag was further applied to over 30 proteins and all but three were sufficiently purified for FCCS analysis. We also observed the interactions between IgG and its binding domain ZZ region (40), and between Smac (second mitochondria-derived activator of caspase or DIABLO) and XIAP (X-linked inhibitor of apoptosis protein, data not shown) (41). Combinations of two affinity tags are expected to help high-throughput purification of the fluorescently labeled proteins, because nickel-chelate beads and streptavidin beads for high-throughput robotic systems are already available from several vendors. Thus, the method presented in this paper should be applicable to a large-scale analysis of protein–protein interactions and should also contribute to the elucidation of protein functions in the post-genomic era.

SUPPLEMENTARY DATA

Supplementary Data are available at NAR Online.

ACKNOWLEDGEMENTS

We thank Megumi Nakamura for the preparation of puromycin derivatives and Yuko Oishi for the preparation of CaM-binding protein plasmid DNAs. This work was supported by Special Coordination Funds of the Science and Technology Agency (Ministry of Education, Culture, Sports, Science and Technology) of the Japanese Government. Funding to pay the Open Access publication charges for this article was provided by Keio University.

Conflict of interest statement. None declared.

REFERENCES

1. Magde,D., Elson,E.L. and Webb,W.W. (1974) Fluorescence correlation spectroscopy. II. An experimental realization. *Biopolymers*, **13**, 29–61.
2. Eigen,M. and Rigler,R. (1994) Sorting single molecules: application to diagnostics and evolutionary biotechnology. *Proc. Natl Acad. Sci. USA*, **91**, 5740–5747.
3. Pack,C.G., Nishimura,G., Tamura,M., Aoki,K., Taguchi,H., Yoshida,M. and Kinjo,M. (1999) Analysis of interaction between chaperonin GroEL and its substrate using fluorescence correlation spectroscopy. *Cytometry*, **36**, 247–253.
4. Wolcke,J., Reimann,M., Klumpp,M., Gohler,T., Kim,E. and Deppert,W. (2003) Analysis of p53 'latency' and 'activation' by fluorescence correlation spectroscopy. Evidence for different modes of high affinity DNA binding. *J. Biol. Chem.*, **278**, 32587–32595.
5. Schwille,P., Meyer-Almes,F.J. and Rigler,R. (1997) Dual-color fluorescence cross-correlation spectroscopy for multicomponent diffusional analysis in solution. *Biophys. J.*, **72**, 1878–1886.
6. Kettling,U., Koltermann,A., Schwille,P. and Eigen,M. (1998) Real-time enzyme kinetics monitored by dual-color fluorescence cross-correlation spectroscopy. *Proc. Natl Acad. Sci. USA*, **95**, 1416–1420.
7. Koltermann,A., Kettling,U., Bieschke,J., Winkler,T. and Eigen,M. (1998) Rapid assay processing by integration of dual-color fluorescence cross-correlation spectroscopy: high throughput screening for enzyme activity. *Proc. Natl Acad. Sci. USA*, **95**, 1421–1426.
8. Kinjo,M., Nishimura,G., Koyama,T., Mets,Ü and Rigler,R. (1998) Single-molecule analysis of restriction DNA fragments using fluorescence correlation spectroscopy. *Anal. Biochem.*, **260**, 166–172.
9. Rigler,R., Foldes-Papp,Z., Meyer-Almes,F.J., Sammet,C., Volcker,M. and Schnetz,A. (1998) Fluorescence cross-correlation: a new concept for polymerase chain reaction. *J. Biotechnol.*, **63**, 97–109.
10. Winkler,T., Kettling,U., Koltermann,A. and Eigen,M. (1999) Confocal fluorescence coincidence analysis: an approach to ultra high-throughput screening. *Proc. Natl Acad. Sci. USA*, **96**, 1375–1378.
11. Doi,N., Takashima,H., Kinjo,M., Sakata,K., Kawahashi,Y., Oishi,Y., Oyama,R., Miyamoto-Sato,E., Sawasaki,T., Endo,Y. *et al.* (2002) Novel fluorescence labeling and high-throughput assay technologies for *in vitro* analysis of protein interactions. *Genome Res.*, **12**, 487–492.
12. Patel,L.R., Curran,T. and Kerppola,T.K. (1994) Energy transfer analysis of Fos-Jun dimerization and DNA binding. *Proc. Natl Acad. Sci. USA*, **91**, 7360–7364.
13. Diebold,R.J., Rajaram,N., Leonard,D.A. and Kerppola,T.K. (1998) Molecular basis of cooperative DNA bending and oriented heterodimer binding in the NFAT1–Fos–Jun–ARRE2 complex. *Proc. Natl Acad. Sci. USA*, **95**, 7915–7920.
14. Haupts,U., Maiti,S., Schwille,P. and Webb,W.W. (1998) Dynamics of fluorescence fluctuations in green fluorescent protein observed by fluorescence correlation spectroscopy. *Proc. Natl Acad. Sci. USA*, **95**, 13573–13578.
15. Kohl,T., Heinze,K.G., Kuhlemann,R., Koltermann,A. and Schwille,P. (2002) A protease assay for two-photon crosscorrelation and FRET analysis based solely on fluorescent proteins. *Proc. Natl Acad. Sci. USA*, **99**, 12161–12166.
16. Kim,S.A., Heinze,K.G., Waxham,M.N. and Schwille,P. (2004) Intracellular calmodulin availability accessed with two-photon cross-correlation. *Proc. Natl Acad. Sci. USA*, **101**, 105–110.
17. Kogure,T., Karasawa,S., Araki,T., Saito,K., Kinjo,M. and Miyawaki,A. (2006) A fluorescent variant of a protein from the stony coral *Montipora* facilitates dual-color single-laser fluorescence cross-correlation spectroscopy. *Nat. Biotechnol.*, **24**, 577–581.
18. Nemoto,N., Miyamoto-Sato,E. and Yanagawa,H. (1999) Fluorescence labeling of the C-terminus of proteins with a puromycin analogue in cell-free translation systems. *FEBS Lett.*, **462**, 43–46.
19. Miyamoto-Sato,E., Takashima,H., Fuse,S., Sue,K., Ishizaka,M., Tateyama,S., Horisawa,K., Sawasaki,T., Endo,Y. and Yanagawa,H. (2003) Highly stable and efficient mRNA templates for mRNA–protein fusions and C-terminally labeled proteins. *Nucleic Acids Res.*, **31**, e78.
20. Hochuli,E., Dobeli,H. and Schacher,A. (1987) New metal chelate adsorbent selective for proteins and peptides containing neighbouring histidine residues. *J. Chromatogr.*, **411**, 177–184.
21. Hofmann,K., Wood,S.W., Brinton,C.C., Montibeller,J.A. and Finn,F.M. (1980) Iminobiotin affinity columns and their application to retrieval of streptavidin. *Proc. Natl Acad. Sci. USA*, **77**, 4666–4668.
22. Oyama,R., Yamamoto,H. and Titani,K. (2000) Glutamine synthetase, hemoglobin alpha-chain, and macrophage migration inhibitory factor binding to amyloid beta-protein: their identification in rat brain by a novel affinity chromatography and in Alzheimer's disease brain by immunoprecipitation. *Biochim. Biophys. Acta*, **1479**, 91–102.
23. Yen,J., Wisdom,R.M., Tratner,I. and Verma,I.M. (1991) An alternative spliced form of FosB is a negative regulator of transcriptional activation and transformation by Fos proteins. *Proc. Natl Acad. Sci. USA*, **88**, 5077–5081.
24. Krouglova,T., Vercammen,J. and Engelborghs,Y. (2004) Correct diffusion coefficients of proteins in fluorescence correlation spectroscopy. Application to tubulin oligomers induced by Mg^{2+} and Paclitaxel. *Biophys. J.*, **87**, 2635–2646.
25. John,M., Leppik,R., Busch,S.J., Granger-Schnarr,M. and Schnarr,M. (1996) DNA binding of Jun and Fos bZip domains: homodimers and heterodimers induce a DNA conformational change in solution. *Nucleic Acids Res.*, **24**, 4487–4494.

26. Kwon,H., Park,S., Lee,S., Lee,D.K. and Yang,C.H. (2001) Determination of binding constant of transcription factor AP-1 and DNA. Application of inhibitors. *Eur. J. Biochem.*, **268**, 565–572.
27. Shirinsky,V.P., Bushueva,T.L. and Frolova,S.I. (1988) Caldesmon–calmodulin interaction. Study by the method of protein intrinsic tryptophan fluorescence. *Biochem. J.*, **255**, 203–208.
28. O'Shea,E.K., Rutkowski,R., Stafford,W.F.,III and Kim,P.S. (1989) Preferential heterodimer formation by isolated leucine zippers from fos and jun. *Science*, **245**, 646–648.
29. Park,J.B., Farnsworth,C.C. and Glomset,J.A. (1997) Ca^{2+}/calmodulin causes Rab3A to dissociate from synaptic membranes. *J. Biol. Chem.*, **272**, 20857–20865.
30. Coppola,T., Perret-Menoud,V., Luthi,S., Farnsworth,C.C., Glomset,J.A. and Regazzi,R. (1999) Disruption of Rab3–calmodulin interaction, but not other effector interactions, prevents Rab3 inhibition of exocytosis. *EMBO J.*, **18**, 5885–5891.
31. Schubert,F., Zettl,H., Hafner,W., Krauss,G. and Krausch,G. (2003) Comparative thermodynamic analysis of DNA–protein interactions using surface plasmon resonance and fluorescence correlation spectroscopy. *Biochemistry*, **42**, 10288–10294.
32. Takano,E., Hatanaka,M. and Maki,M. (1994) Real-time-analysis of the calcium-dependent interaction between calmodulin and a synthetic oligopeptide of calcineurin by a surface plasmon resonance biosensor. *FEBS Lett.*, **352**, 247–250.
33. Heuer,K.H., Mackay,J.P., Podzebenko,P., Bains,N.P., Weiss,A.S., King,G.F. and Easterbrook-Smith,S.B. (1996) Development of a sensitive peptide-based immunoassay: application to detection of the Jun and Fos oncoproteins. *Biochemistry*, **35**, 9069–9075.
34. Levine,S.S., King,I.F. and Kingston,R.E. (2004) Division of labor in polycomb group repression. *Trends Biochem. Sci.*, **29**, 478–485.
35. Hashimoto,N., Brock,H.W., Nomura,M., Kyba,M., Hodgson,J., Fujita,Y., Takihara,Y., Shimada,K. and Higashinakagawa,T. (1998) RAE28, BMI1, and M33 are members of heterogeneous multimeric mammalian polycomb group complexes. *Biochem. Biophys. Res. Commun.*, **245**, 356–365.
36. Alkema,M.J., Bronk,M., Verhoeven,E., Otte,A., van't Veer,L.J., Berns,A. and van Lohuizen,M. (1997) Identification of Bmi1-interacting proteins as constituents of a multimeric mammalian polycomb complex. *Genes Dev.*, **11**, 226–240.
37. Levine,S.S., Weiss,A., Erdjument-Bromage,H., Shao,Z., Tempst,P. and Kingston,R.E. (2002) The core of the polycomb repressive complex is compositionally and functionally conserved in flies and humans. *Mol. Cell. Biol.*, **22**, 6070–6078.
38. García,E., Marcos-Gutiérrez,C., del Mar Lorente,M., Moreno,J.C. and Vidal,M. (1999) RYBP, a new repressor protein that interacts with components of the mammalian polycomb complex, and with the transcription factor YY1. *EMBO J.*, **18**, 3404–3418.
39. Angus,S.P., Solomon,D.A., Kuschel,L., Hennigan,R.F. and Knudsen,E.S. (2003) Retinoblastoma tumor suppressor: analyses of dynamic behavior in living cells reveal multiple modes of regulation. *Mol. Cell. Biol.*, **23**, 8172–8188.
40. Nilsson,B., Moks,T., Jansson,B., Abrahmsen,L., Elmblad,A., Holmgren,E., Henrichson,C., Jones,T.A. and Uhlen,M. (1987) A synthetic IgG-binding domain based on staphylococcal protein A. *Protein Eng.*, **1**, 107–113.
41. Du,C., Fang,M., Li,Y., Li,L. and Wang,X. (2000) Smac, a mitochondrial protein that promotes cytochrome *c*-dependent caspase activation by eliminating IAP inhibition. *Cell*, **102**, 33–42.

Microenvironment and Effect of Energy Depletion in the Nucleus Analyzed by Mobility of Multiple Oligomeric EGFPs

Changi Pack, Kenta Saito, Mamoru Tamura, and Masataka Kinjo
Laboratory of Supramolecular Biophysics, Research Institute for Electronic Science, Hokkaido University, Sapporo 060-0812, Japan

ABSTRACT Four different tandem EGFPs were constructed to elucidate the nuclear microenvironment by quantifying its diffusional properties in both aqueous solution and the nuclei of living cells. Diffusion of tandem EGFP was dependent on the length of the protein as a rod-like molecule or molecular ruler in solution. On the other hand, we found two kinds of mobility, fast diffusional mobility and much slower diffusional mobility depending on cellular compartments in living cells. Diffusion in the cytoplasm and the nucleoplasm was mainly measured as fast diffusional mobility. In contrast, diffusion in the nucleolus was complex and mainly much slower diffusional mobility, although both the fast and the slow diffusional mobilities were dependent on the protein length. Interestingly, we found that diffusion in the nucleolus was clearly changed by energy depletion, even though the diffusion in the cytoplasm and the nucleoplasm was not changed. Our results suggest that the nucleolar microenvironment is sensitive to energy depletion and very different from the nucleoplasm.

INTRODUCTION

The cell nucleus contains many proteins that form a multimolecular complex or a material such as chromatin and a nucleolus. Most of the proteins in the nucleus are concerned with molecular processing such as ribosome biogenesis, mRNA synthesis, transcription and molecular transportation to and from the nucleus. For these processes to be accomplished properly, proteins related to each process are expected to act dynamically and precisely in the nucleus. Consequently, the dynamics of various molecules such as RNAs and nuclear proteins in living cells have become a subject of major interest because mobilities of such molecules in the nucleus could provide important information about the molecular functions of the nucleus (1–3). On the other hand, such mobility of functional protein molecules in the nucleus might be mainly affected by the nuclear architecture and microenvironment (1,4) as well as their function because the chromosomes and the nucleoli occupy a large portion of the nuclear space and changes depending on many factors such as gene expression, cell cycle progression, and other metabolic state of the cell. Therefore, for understanding the relation between functional proteins and nuclear microenvironment, it is helpful to analyze mobility of standard protein molecules with well-defined hydrodynamic properties as well as functional nuclear proteins (1,5,6) or labeled macromolecules (7).

In the last few years, many studies based on fluorescence microscopic techniques such as FRAP, single particle tracking (SPT), and fluorescence correlation spectroscopy (FCS) have been carried out for cell biology (8–15). The studies showed that a variety of small fluorescent probes such as BCECF (9), fluorescein-labeled macromolecules (dextran and Ficoll) from 3 to 1000 kD (13), and monomeric EGFP (14), move rapidly in the cytoplasm, whereas labeled linear dsDNA diffuses very slowly and has a size dependence of the diffusion constant (16). The key point of these studies is that the diffusion of small dextrans and Ficolls in the cytoplasm is only restricted mildly whereas that for large macromolecules can be greatly slowed.

On the other hand, a few studies of protein mobility in the cell nucleus have been carried out (10,13,14) with biologically inert protein, even though many studies have been carried out with nuclear proteins (1,3,6). A study based on FRAP and microinjection with diverse sizes of fluorescein-labeled dextrans (13) showed that diffusion in the nucleus was slowed approximately fourfold compared with their diffusion in water. However, more variability in the measured data for the nucleus was found than for cytoplasm. Monomer GFP molecule showed much more complex diffusion in nucleus than in cytoplasm (14). Recent studies of FRAP (1,17) and FCS combined with FRAP experiment (18) using living cells have shown that various EGFP-fused nuclear proteins diffuse at different rates depending on their localization and function. Nuclear proteins could interact with target molecules or immobile structures such as chromatin, which slowed down the mobility of the proteins (5,6,19). An FCS experiment with monomeric EGFP showed that diffusion of EGFP, which is presumably inert to other proteins, was restricted depending on the position in the nucleus compared to diffusion in the cytoplasm (14). Furthermore, whether intranuclear mobility of many molecules results from passive diffusion or active

Submitted December 9, 2005, and accepted for publication August 11, 2006.

Address reprint requests to Masataka Kinjo, Laboratory of Supramolecular Biophysics, R.I.E.S, Hokkaido University, N12W6, Kita-Ku, Sapporo 060-0812, Japan. Tel.: 81-11-7062890; Fax: 81-7064964; E-mail: kinjo@imd.es.hokudai.ac.jp.

Abbreviations used: cps, count per second; Cyt, cytoplasm; 2-DG, 2-deoxyglucose; DT, diffusion time; $EGFP_n$, tandemly linked oligomeric EGFP; FAF, fluorescence autocorrelation function; MR, molecular ruler; FCS, fluorescence correlation spectroscopy; FRAP, fluorescence recovery after photobleach; mRFP, monomeric red fluorescent protein; NP, nucleoplasm; NL, nucleolus; SPT, single particle tracking; TSA, Trichostatin A.

0006-3495/06/11/3921/16 $2.00

doi: 10.1529/biophysj.105.079467

transport is still controversial (3,20). The nuclear microenvironment, which may be one of the reasons, has not yet been clearly quantified under various physiological conditions.

FCS has been applied as a powerful technique for assessing biomolecular diffusion and interactions both in aqueous conditions and in living cells with single-molecule sensitivity (21–26). FCS detects fluorescence intensity fluctuations caused by Brownian motion of fluorescent probe molecules in a tiny detection volume (~0.3 fL) generated by confocal illumination. Through time correlation analysis of the fluorescence fluctuations, the diffusion coefficient, the molecular concentration, and the molecular interaction of probe molecules are accessible. Because FCS need only a very small detection volume and has high sensitivity, it will also be useful to measure diffusional mobility of proteins in very small regions of subnuclear microenvironments in living cells. Although FRAP is adequate for measuring the diffusion of fluorescent molecules and possible exchange in target organelles in the living cell (3,7), the measurable minimal fluorescent intensity and diffusional speed range are limited to brighter and slower ranges than those for FCS. Therefore, we can anticipate that FCS will provide complementary information for faster movement at lower expression levels of various functional proteins in the nucleus.

EGFP is a powerful fluorescent bioprobe molecule with a well-known cylindrical structure (27–29). It has recently been used for various cell measurements in fluorescent imaging of cells as well as for analysis of molecular diffusion using FRAP and FCS. To develop a standard and reproducible method for diffusion analysis of proteins, we designed multiple oligomeric EGFPs with different molecular weights, which can be used as molecular rulers (MRs) for quantification of protein mobility in the nucleus. For this purpose, we constructed plasmids with different levels of oligomeric $EGFP_n$ ($EGFP_2$–$EGFP_5$, $n = 2$–5) with molecular weights of 60, 90, 120, and 150 kD, respectively, tandemly linked by a random amino acid linker. Using multiple oligomeric EGFPs and FCS, we determined the diffusion of the proteins in the cytoplasm, nucleoplasm, and nucleoli of living HEK293, HeLa, and COS7 cells. For strict recognition of the two compartments in the nucleus, mRFP-fibrillarin and H2B-mRFP were used as red fluorescent markers for the nucleolus and the nucleoplasm, respectively.

In this study, FCS analysis by a one-component model showed that the diffusional mobility of $EGFP_n$ in aqueous solution was dependent on the length of $EGFP_n$ and was well consistent with the diffusion model of a rod-like structure. On the other hand, the diffusion of $EGFP_n$ in living cells analyzed by a two-component model showed that fast diffusional mobility in the cytoplasm and the nucleoplasm was consistent with the model of a rod-like molecule as shown in aqueous solution. The fast diffusion rates in the cytoplasm and the nucleoplasm were almost the same, and ~3.5-fold slower than in solution, regardless of the size of tandem $EGFP_n$ and cell type. Mobilities of tandem $EGFP_n$ found in the nucleoli of HeLa and COS7 cells were fivefold and sevenfold slower than the fast diffusional mobility in the cytoplasm and the nucleoplasm, respectively. Moreover, the much slower diffusional mobility in the nucleolus was also dependent on the length of $EGFP_n$, demonstrating tandem EGFP molecules were well-defined both in solution and in living cells. Interestingly, the slow diffusion in the nucleolus was related to the energy level of the living cell, because the slow diffusion of $EGFP_5$ in the nucleolus, but not in the cytoplasm and the nucleoplasm, was further slowed by ATP depletion.

MATERIALS AND METHODS

Plasmid construction of tandem EGFP

Plasmids expressing each tandem $EGFP_n$ were synthesized with the plasmid expressing EGFP-C1 (Clontech, Palo Alto, CA). The EGFP-C1 was excised at the *NdeI* and the *SmaI* restriction sites and ligated between the *NdeI* and *Eco*47 III restriction sites of another EGFP-C1. The linker between $EGFP_n$ containing 25 random amino acid residues (SGLRSRAQASNSAVDGTAGPLPVAT) originated from the remaining bases of the multiple-cloning site. Plasmid constructs of H2B-mRFP and mRFP-fibrillarin were obtained as gifts from Drs. H. Kimura (Kyoto University, Kyoto, Japan) (30,31) and T. Saiwaki (Osaka University, Osaka, Japan) (32), respectively. All plasmid constructs for transfection were purified using a plasmid DNA midiprep kit (QIAGEN, Hilden, Germany).

Cell culture and expression of tandem $EGFP_n$ proteins

For transient expression of tandem $EGFP_n$, human embryonic kidney 293 (HEK293), HeLa, and COS7 cells were plated at confluence levels of 10–20% on LAB-TEK chambered coverslips with eight wells (Nalge Nunc International, Rochester, NY) for 12 or 24 h before transfection. Cells were transfected with a $EGFP_n$ vector or cotransfected with a vector of $EGFP_n$ and H2B-mRFP or mRFP-fibrillarin, and grown in a 5% CO_2 humidified atmosphere at 37°C in Dulbecco's modified Eagle's medium (DMEM, Sigma-Aldrich, St. Louis, MO) supplemented with 10% fetal bovine serum, 100 U/ml penicillin, and 10 mg/ml streptomycin. Transfection was carried out with FuGENE 6 (Roche Molecular Biochemicals, Mannheim, Germany) or Effectene (QIAGEN) as indicated by the manufacturer. The transfected cells were incubated for 24 or 48 h and washed with Opti-MEM to remove phenol red dye in DMEM, and then the medium was replaced by Opti-MEM before LSM and FCS measurements. Energy depletion was performed by addition of 6 mM 2-deoxyglucose (2-DG, Sigma-Aldrich) and 10 mM sodium azide (NaN_3, Sigma) to the culture medium (3,20). LSM images were collected for the same cells before and after 2-DG and NaN_3 treatment.

Western immunoblotting

The immunoblot analysis was performed according to the standard method. Cells expressing tandem $EGFP_n$ were grown on 10-cm culture plates for 48 h after transfection, the BD Living Colors A.v. peptide antibody (BD Biosciences Clontech, Mountain View, CA) was used as the primary antibody. Primary antibody-bound protein bands were detected with an alkaline phosphatase-conjugated secondary antibody (mouse anti-rabbit IgG, Chemicon International, Temecula, CA) by BCIP/NBT dye solution (Sigma-Aldrich).

Cell homogenization

After FCS measurements, the cultured cells on a Lab-Tek (Nalge Nunc International) chambered coverslip were collected by centrifugation at

1500 rpm for 5 min and then the pellets of cells were homogenized in 50 μl of buffer (10 mM Hepes pH 7.9 containing 10 mM NaCl, 3 mM MgCl2, 1 mM DTT, 0.4 mM PMSF, and 0.1 mM sodium orthovanadate). Each $EGFP_n$ protein solution was collected from the supernatant after centrifugation at 100,000 rpm for 20 min and measured by FCS again.

Live cell imaging

Fluorescence microscopy was performed using an LSM510 inverted confocal laser scanning microscopy (LSM; Carl Zeiss, Jena, Germany). LSM observations were all performed at 25°C. $EGFP_n$ was excited at 488 nm of a CW Ar^+ laser through a water immersion objective lens (C-Apochromat, 40×, 1.2 NA; Carl Zeiss) with emission detected above 505 nm for single scanning experiments using cells expressing $EGFP_n$. Monomeric RFP-fibrillarin or H2B-mRFP was imaged using a 543-nm laser light and detection was above 560 nm. The pinhole diameters for confocal imaging were adjusted to 70 μm and 80 μm for EGFP and mRFP, respectively. To avoid bleed-through effects in double-scanning experiments, EGFP and mRFP were scanned independently in a multitracking mode.

FCS measurements and quantitative analysis

FCS measurements were all performed at 25°C on a ConfoCor 2 (Carl Zeiss) as described previously (24,33). Excitation of EGFP was carried out at 488 nm and 6.3 mW by adjusting an acousto-optical tunable filter (AOTF) to 0.1%. Fluorescence autocorrelation functions ((FAF) $G(\tau)$), from which the average residence time (τ_i) and the absolute number of fluorescent proteins in the detection volume were obtained as follows:

$$G(\tau) = \frac{\langle I(t)I(t+\tau)\rangle}{\langle I(t)\rangle^2}, \tag{1}$$

where $I(t+\tau)$ is the fluorescence intensity in single photon counting method obtained from the detection volume at delay time τ. Brackets denote ensemble averages. The curve fitting for the multicomponent model is given by:

$$G(\tau) = 1 + \frac{1}{N}\sum_i y_i \left(1+\frac{\tau}{\tau_i}\right)^{-1}\left(1+\frac{\tau}{s^2\tau_i}\right)^{-1/2}, \tag{2}$$

where y_i and τ_i are the fraction and diffusion time of component i, respectively. N is the number of fluorescent molecules in the detection volume defined by the beam waist w_0 and the axial radius z_0, s is the structure parameter representing the ratio of w_0 and z_0. The detection volume made by w_0 and z_0 was approximated as a cylinder.

All FAFs in aqueous solutions were measured for 30 s five times at 5-s intervals. In the case of intracellular measurement, FAFs were measured for 15 s one or three times, and very low fluorescent cells under concentration of 20 molecules (<0.1 M) per detection volume (0.3 fL) were chosen for FCS measurement. Under these conditions, the effect of photobleaching on FCS analysis was minimized. The measurement position was chosen in the LSM image. Because the optical passes of LSM and FCS are not the same, the real position of FCS measurement was tuned to the position on LSM images with a coverglass coated by dried rhodamine 6G (Rh6G), following the protocol provided by the manufacturer (34). The real position of FCS measurement was also checked with bleaching of H2B-mRFP in living cells. Although there was no significant difference between the position of FCS measurements checked by a coverglass and living cells, misalignment under 1 μm was found. This range of misalignment may not affect analysis of diffusion in the region of nucleoplasm and nucleolus, diameters of which were of the order of 10 and 2 μm, respectively. The detection pinhole for FCS was fixed to a diameter of 70 μm and emission was recorded through a 505–550-nm bandpass filter for measurement of cells expressing $EGFP_n$ or through a 505–530-nm bandpass filter for measurement of cells coexpressing $EGFP_n$ and mRFP tagged proteins for excluding any cross-talk signal from mRFP. In practice, there was almost no cross-talk signal from mRFP using the three cell types expressing mRFP only. The fluorescence of cells expressing mRFP shows almost the same background fluorescence signal under 15 cps when a 505–550-nm bandpass filter was used. All measured FAFs were fitted by the fit program installed on the ConfoCor 2 system using the model Eq. 2. FAFs in aqueous solutions were fitted by a one-component model ($i = 1$), and FAFs in cells by a one- or two-component model ($i = 1$ or 2) to consider free diffusion and restricted diffusion, respectively (see also the text). The pinhole adjustment of the FCS setup, structure parameter, and detection volume were calibrated everyday by FCS measurements of Rh6G solution with a concentration of 10^{-7} M. Although the structure parameters determined by Rh6G after the pinhole adjustment were changed and ranged from 4 to 8 each day, FCS analysis was carried out with data sets with structure parameters ranging from 5 to 6, which are known to be a stable condition for FCS measurement. An average value of structure parameter was fixed for FCS analysis of all data carried out in a day under the same conditions. Diffusion time of component i, τ_i, is related to the translational diffusion constant D of component i by

$$\tau_i = \frac{w^2}{4D_i}. \tag{3}$$

Diffusion of a spheroidal molecule is related to various physical parameters by the Stokes-Einstein equation as follows

$$D_i = \frac{\kappa_B T}{6\pi\eta r_i}, \tag{4}$$

where T is the absolute temperature, r_i is the hydrodynamic radius of the spheroidal molecule, η is the fluid-phase viscosity of the solvent, and k_B is the Boltzman constant. Because τ_i is proportional to viscosity, the relative viscosity ($\tau_{cell}/\tau_{solution}$) can be easily estimated. When the diffusion time of Rh6G is measured and the molecular weight of the sample molecule is known, the diffusion time of the sample molecule as a spherical shape can be simply calculated by the following equation (23).

$$\tau_{sphere} = \tau_{Rh6G}\left(\frac{MW_{sphere}}{MW_{Rh6G}}\right)^{1/3}. \tag{5}$$

The diffusion time τ is also related to the frictional coefficient of the diffusing molecules, which depends on the shapes of molecules undergoing diffusion in a solution of defined viscosity. The ratio of the frictional coefficient between spheroidal (f_0) and ellipsoidal (f) molecules and the relationship between the diffusion time and frictional coefficient are given by Perrin's equation (35,36)

$$\frac{f}{f_0} = \frac{(p^2-1)^{1/2}}{p^{1/3}\ln(p+(p^2-1)^{1/2})} \tag{6}$$

$$\tau_{ellips} = \tau_{sphere}\frac{f}{f_0}, \tag{7}$$

where f and f_0 are frictional coefficients of ellipsoidal and spherical molecules, respectively, p is the axial ratio of the ellipsoidal molecule, τ_{ellips} and τ_{sphere} are the diffusion times of ellipsoidal and spherical molecules, respectively. Based on the known size of the EGFP molecule, 4 nm in length and 3 nm in diameter, and the average length of 25 amino acids, the predicted diffusion time of tandem $EGFP_n$ was calculated for spherical and ellipsoidal models using Eqs. 5, 6, and 7. The lengths of amino acid linkers used for the calculation were 3.7 nm for an α-helix structure and 9.1 nm for a simple linear structure of 25 amino acids. The diffusion constants of $EGFP_n$s (D_{gfpn}) in the solution and cells were calculated from the published diffusion constant of Rh6G, D_{Rh6G} (280 $\mu m^2/s$) (37), and measured diffusion times of Rh6G (τ_{Rh6G}) and $EGFP_n$s (τ_{gfpn}) as follows:

$$\frac{D_{gfpn}}{D_{Rh6G}} = \frac{\tau_{Rh6G}}{\tau_{gfpn}}. \tag{8}$$

RESULTS

LSM observation

Expressed oligomeric $EGFP_n$ localized in the nucleus

To observe the distribution and localization of monomer EGFP and oligomeric $EGFP_n$ in HEK293, COS7, and HeLa cells, the cells were transiently transfected with DNA plasmids encoding $EGFP_n$ or cotransfected with plasmids encoding each $EGFP_n$ and H2B-mRFP. Cells expressing each oligomeric EGFP were observed at 24–48 h after transfection. Typical LSM images of HeLa cells expressing each $EGFP_n$ taken at 24 h after transfection are shown in Fig. 1. Monomer EGFP and $EGFP_2$ were uniformly distributed through the cytoplasm and nucleus in each cell except in the nucleolus (Fig. 1 *A* (*F*) and *B* (*G*)). In contrast, $EGFP_3$, $EGFP_4$, and $EGFP_5$ showed different distribution patterns in the cytoplasm and the nucleus. In the case of $EGFP_3$, the fluorescent intensity of proteins in the cytoplasm was higher than that in the nucleus, although the difference was not significant (Fig. 1, *C* and *H*). For $EGFP_4$ and $EGFP_5$, the fluorescent intensity in the nucleus was much weaker than that in the cytoplasm (Fig. 1 *D* (*I*) and *E* (*J*)). However, the fluorescence intensity of $EGFP_4$ and $EGFP_5$ in the nucleus was sufficient to be detected by LSM measurement (Fig. 1, *I* and *J*). The fluorescent intensities in the nucleus for $EGFP_2$, $EGFP_3$, $EGFP_4$, and $EGFP_5$ at 48 h were increased compared with these at 24 h. For all oligomeric $EGFP_n$, there was no speckled or aggregated distribution in the cytoplasm and the nucleoplasm and the fluorescence in the nucleoplasm except in the nucleolus had a uniform pattern (Fig. 1, *F–J*). This uniform pattern of fluorescence in the nucleoplasm was confirmed by comparing the fluorescence of tandem EGFP with that of H2B-mRFP on HeLa or COS7 cells coexpressing $EGFP_3$ and H2B-mRFP or $EGFP_5$ and H2B-mRFP, respectively (Fig. S1 in Supplementary Material), because it is known that H2B-GFP show heterogeneous fluorescent pattern in the nucleus depending on the density of chromatin (4,31,38). In the case of HEK293 and COS7 cells transfected with the tandem $EGFP_n$, the difference of fluorescence intensity between the cytoplasm and nucleus was clearly discriminated from $EGFP_3$ regardless of the expression level, and the fluorescent intensity in the nucleus was decreased with the increase in size of tandem GFP (C. Pack and M. Kinjo, unpublished data).

LSM observations of HeLa cell indicated that tandem EGFP bigger than $EGFP_3$ (>90 kD) had difficulty localizing in the nucleus. The localization of $EGFP_n$ in the nucleus was dependent on the size of the $EGFP_n$ molecule. Although all types of tandem GFP_n could be localized in the nucleus, there was less tandem $EGFP_4$ and $EGFP_5$ in the nucleus than monomeric EGFP, $EGFP_2$, and $EGFP_3$. The small number of EGFP molecules in the nucleus (from 50 to 5 molecules in the detection volume of 0.3 fL) might be sufficient to be detected by FCS measurement even in very weak fluorescent cells. For the weak fluorescent intensity in the nucleus for $EGFP_3$, $EGFP_4$, and $EGFP_5$, we did not need to select weakly expressing cells as explained in Materials and Methods, and could easily perform FCS measurement in the nucleus.

FCS measurement in aqueous solution

Tandem $EGFP_n$ diffuse in solution like a rod-like molecule

For analysis of the diffusion properties of monomer EGFP and oligomeric $EGFP_n$ in aqueous solution, cells transfected

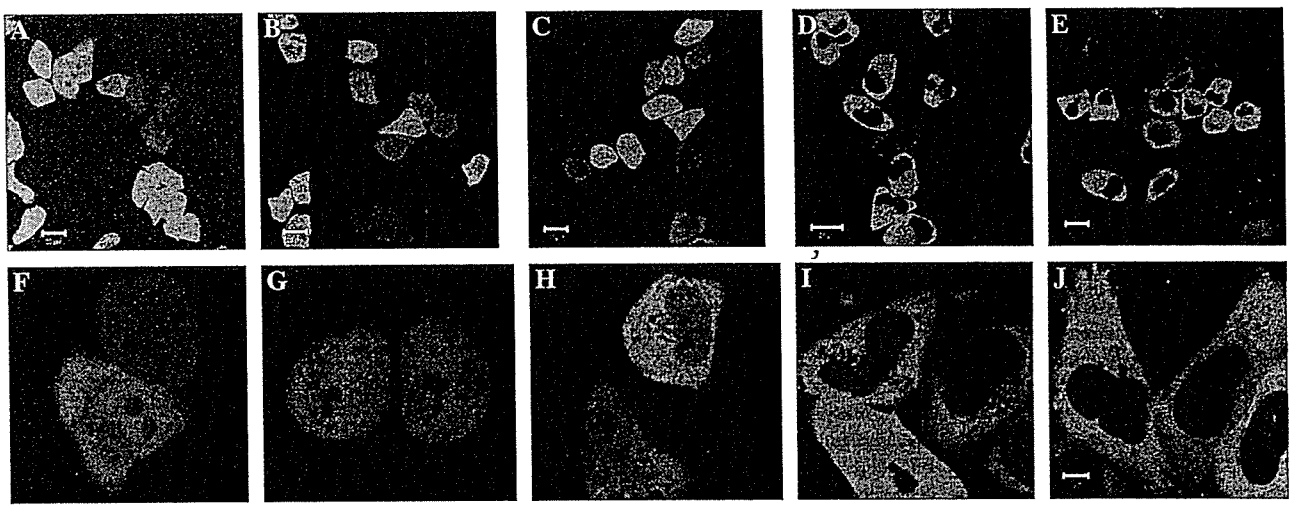

FIGURE 1 Tandem EGFP located in the nucleus. LSM images of HeLa cells expressing (*A*) monomer EGFP, (*B*) $EGFP_2$, (*C*) $EGFP_3$, (*D*) $EGFP_4$, and (*E*) $EGFP_5$, are shown. The images were taken at 24 h and 48 h after transfection with EGFP and tandem $EGFP_n$, respectively. Bars, 20 μm. Panels *F* and *J* show enlarged images of cells expressing $EGFP_n$ from $EGFP_1$ to $EGFP_5$, respectively, showing their location on the nucleus. Bars, 10 μm. The fluorescent intensity in the nucleus decreased with the increase in size of the oligomers. Tandem EGFPs, regardless of their size, were equally distributed in the nucleoplasm except the nucleolus (see also supplementary Fig. S1).

with the $EGFP_n$ were homogenized and the proteins from the cell lysate were extracted and measured in aqueous solution. There was no drastic change or burst of average fluorescent intensity during FCS measurement resulting from aggregated EGFP molecules or contaminants from the homogenized cell extracts during the measurement time of 60 s. The FAF of each tandem $EGFP_n$ was analyzed by a one-component model (Eq. 2, $i = 1$) and was well fitted. Fig. 2 *A* shows typical FAFs of $EGFP_n$ obtained from aqueous solution. For comparison of the extents of diffusion speeds, the amplitude of $G(\tau)$ ($G(0) - 1$) was normalized to unity. The autocorrelation functions of $EGFP_n$ shifted gradually to the right depending on the molecular weight of tandem $EGFP_n$ (Fig. 2 *B*). Diffusion times corresponding to the FAFs of $EGFP_{1\sim5}$ were 86.8 ± 3.9 μs, 125.8 ± 2.7 μs, 147.4 ± 4.8 μs, 185.4 ± 5.4 μs, and 200 ± 8.5 μs, respectively (Fig. 2 *C*). These results indicated that the diffusional mobility of $EGFP_n$ decreased with increasing molecular weight. That there was no degradation of monomeric and tandem $EGFP_n$ was also confirmed by the Western blotting results (Fig. 2 *B*), which were well consistent with the expected molecular weight of each oligomeric $EGFP_n$. Diffusion constants of monomeric and oligomeric $EGFP_n$ in solution are summarized in Fig. 2 *D*. The diffusion constant (76 $\mu m^2 s^{-1}$) of monomeric EGFP (263 amino acids, 30 kD) was similar to those (87 $\mu m^2 s^{-1}$) of previous studies (24,39,40) with recombinant GFP (238 amino acids, 27 kD) synthesized by bacterial expression.

Oligomeric $EGFP_n$ contains a linker of 25 random amino acids connecting monomer EGFP molecules. Consequently, oligomeric $EGFP_n$ can have different molecular shapes from spherical to linear. Because the linker can change p, the axial ratio of the protein molecule (Eq. 6), the diffusional mobilities of tandem types of $EGFP_n$ from $EGFP_2$ to $EGFP_5$ may reflect the diffusional mobility of an ellipsoidal or rod-like molecule. For this case, diffusion times of oligomeric $EGFP_n$ from $EGFP_2$ to $EGFP_5$ could be much slower than those of the proteins in spherical shape. Fig. 2 *C* shows a plot of the measured diffusion time (*solid circles*) of each EGFP and three plots of predicted diffusion times calculated by diffusion models for the spherical shape and two rod-like shapes with different p-values (Eqs. 5–7). Enhanced EGFP has a well-known cylindrical structure with a diameter of ~3 nm and height of ~4 nm (27). For simplification, monomer EGFP was assumed to be a spherical molecule and then the diffusion time of oligomeric $EGFP_n$ was calculated as a spherical molecule or rod-like molecule by Eq. 5. The measured diffusion time of monomer EGFP (30 kD) agreed well with the calculated value obtained from Eq. 5 using the empirical diffusion time (21 ± 2 μs) and the known molecular weight (0.479 kD) of Rh6G. The dashed line in Fig. 2 *C* plots the calculated diffusion time of oligomeric $EGFP_n$ with a spherical shape. The other two lines plot the predicted diffusion times of rod-like oligomeric $EGFP_n$ assuming that the amino acid linkers have an α-helix (*solid line*) or a linear structure (*dotted line*) with lengths of ~3.7 nm and ~9.1 nm, respectively. With this simple assumption, $EGFP_{1\sim5}$ have longitudinal lengths of 4, 12, 20, 28, and 36 nm, respectively, for an α-helix linker and 4, 17, 30, 43, and 56 nm, respectively, for a linear linker. As shown in Fig. 2 *C*, the measured diffusion times of oligomeric $EGFP_n$ (*solid circles*) are much longer than the calculated diffusion times of

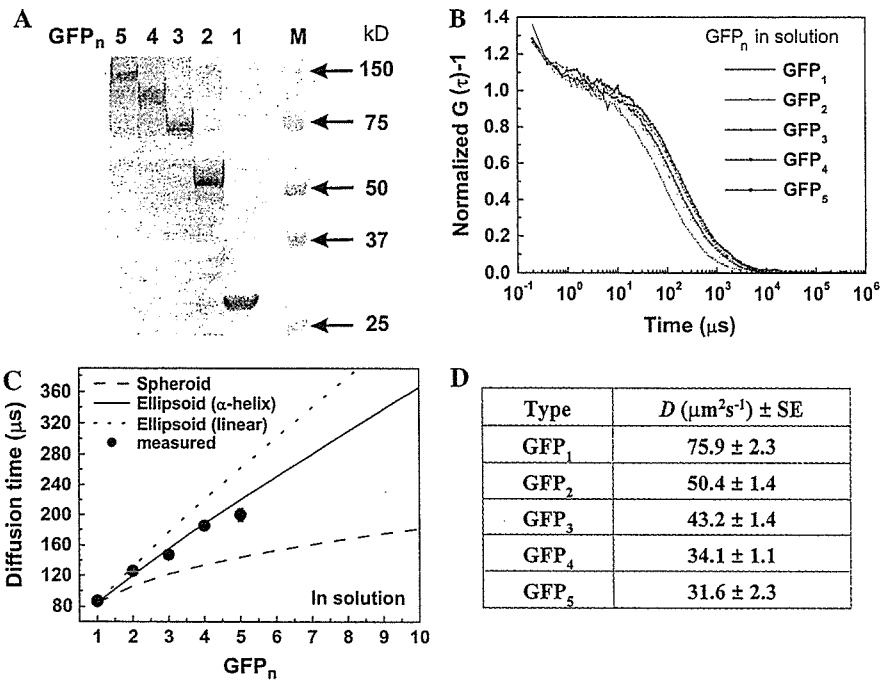

D

Type	D ($\mu m^2 s^{-1}$) ± SE
GFP_1	75.9 ± 2.3
GFP_2	50.4 ± 1.4
GFP_3	43.2 ± 1.4
GFP_4	34.1 ± 1.1
GFP_5	31.6 ± 2.3

FIGURE 2 FCS measurement of tandem $EGFP_n$ in aqueous solution. (*A*) Immunoblots of EGFP and tandem $EGFP_n$ and (*B*) normalized FAFs of the proteins in aqueous solution are shown. Lysates from HEK293 cells expressing monomer EGFP and oligomer $EGFP_n$ were blotted. The amplitude of FAF, $G(0) - 1$, was normalized to unity for comparison of the extent of diffusional speed. Diffusion times obtained by fitting the functions (*B*) with a one-component model (Eq. 2, $i = 1$) are plotted in panel *C*. Error bar shows mean ± SD of three measurements. Dashed line shows diffusion times calculated by Eq. 5 using the molecular weight and the measured diffusion time of Rh6G assuming the oligomeric $EGFP_n$ is spherical. Solid and dotted lines show the calculated diffusion times assuming that the linker between EGFP forms a rigid α-helix and a linear shape, respectively. (*D*) Diffusion constants for EGFP and tandem $EGFP_n$ in aqueous solution. Each diffusion constant was calculated from Eq. 8 using the known diffusion constant (280 $\mu m^2 s^{-1}$) and the measured diffusion time (21 ± 2 μs) of Rh6G. Data are averaged from five independent experiments. (Mean ± SE of five independent experiments.)

the $EGFP_n$ as a spherical molecule and well agreed with the rod-like model for the α-helix linker, even though the diffusion time of $EGFP_5$ was slightly shorter than the calculated value. This indicated that diffusion of monomer and oligomeric $EGFP_n$ from $EGFP_2$ to $EGFP_5$ in solution reflected free diffusion of rod-like molecules and depended on the putative length of the oligomeric EGFP. Consequently, we concluded that monomeric and oligomeric $EGFP_n$ could be used as molecular rulers that change the diffusion time according to their own longitudinal length. This property of tandem $EGFP_n$ will be useful to analyze mobility of proteins in organelles, particularly in the subnuclear microenvironment.

LSM and FCS measurement in cells

FCS measurements of oligomeric $EGFP_n$ in vivo were performed using three cell lines, HEK293, COS7, and HeLa. Cells expressing a comparatively low concentration of $EGFP_n$ under ~20 molecules (<0.1 μM) per detection volume (0.3 fL) were chosen because a dilute concentration of fluorescent molecules is adequate for FCS measurement. Even with this condition, there might be photobleaching effect on FCS measurements. Recently, a method combining FCS with photobleaching analysis was reported for studying intracellular binding and diffusion of functional proteins (41). This study suggested that the method is applicable to analyze mobility of monomer EGFP even in highly fluorescent cells. Nevertheless, it is noted that our study focused on the mobility of freely moving tandem $EGFP_n$ in the microenvironment containing the detection volume, but not that of immobile tandem $EGFP_n$, which gives rise to a photobleaching and make FCS analysis more complex. For excluding a possible photobleaching effect, we carefully selected cells with weak fluorescence or without photobleaching during FCS measurement.

All FCS measurements were performed after taking LSM images and multiple positions for FCS measurements in the cytoplasm excepting endoplasmic reticulum and plasma membrane, and multiple positions in the nucleus were chosen in the LSM image of a cell. After FCS measurements, an LSM image was taken again to check whether measured positions of FCS were deviated from the LSM images. In weakly fluorescent cells, it was not easy to discriminate the nucleolus from the nucleoplasm, particularly, in cells expressing $EGFP_3$, $EGFP_4$, and $EGFP_5$, in which most of the proteins were located in the cytoplasm and only a few EGFP molecules were located in the nucleus. Fig. 3 shows typical examples of LSM and FCS measurements for the three cell lines. LSM images for FCS measurement of a HEK cell expressed by $EGFP_1$, a COS7 cell by $EGFP_4$, and a HeLa cell by $EGFP_5$ are shown in Fig. 3, *A*, *C*, and *E*, respectively. On the weakly fluorescent HEK cell expressing EGFP (Fig. 3 *A*), the boundary between the cytoplasm and nucleus was not clear. On the other hand, the cells expressing $EGFP_4$, and $EGFP_5$ (Fig. 3, *C* and *E*) show a clear contrast of the boundary resulting from the difference of fluorescence intensity between the cytoplasm and nucleus. The boundary between the cytoplasm and nucleus was not clear for weakly fluorescent cells expressing $EGFP_1$ and $EGFP_2$, regardless of the cell type. However, the boundary was clearly visible with cells expressing $EGFP_3$, $EGFP_4$, and $EGFP_5$, depending on the size of tandem $EGFP_n$, even though the fluorescence signals of the cells were weak. The clear boundary between the cytoplasm and nucleus for $EGFP_3$, $EGFP_4$, and $EGFP_5$ made it easy to discriminate the two.

FCS analysis in living cells

For all cells expressing $EGFP_1$ or tandem $EGFP_n$, diffusive fluorescent regions in the cytoplasm and multiple positions in the nucleus were measured by FCS. Examples of FAFs of EGFP in HEK, $EGFP_4$ in COS7, and $EGFP_5$ in HeLa cells are shown in Fig. 3, *B*, *D*, and *F*, respectively. Cross-hairs in the LSM images correspond to the FCS measurement points. In Fig. 3 *B*, position 1 of FCS measurement point was chosen for measuring cytoplasm, and positions 2 and 3 were presumed to be in the nucleus. In Fig. 3, *D* and *F*, position 1 of the cross-hair corresponds to a point in the cytoplasm and positions 2 and 3 to random points in the nucleus. The amplitudes of all FAF ($G(0) - 1$) were normalized to unity for comparison of the shift of the curve. One of two FAFs obtained from the nucleus showed no or a small difference from that in the cytoplasm (curve *2* in Fig. 3, *B*, *D*, and *F*). Interestingly, other FAFs obtained from the nucleus largely shifted to the right, indicating much slower diffusional mobility (curve *3* in Fig. 3, *B*, *D*, and *F*). This slower diffusion was occasionally found in nuclei of all cells expressing monomeric and oligomeric $EGFP_n$ regardless of the cell type. This indicated that there were two types of diffusional mobility in the three compartments: the fast-diffusion-mobility (FAF curves *1* and *2* in Fig. 3) in the cytoplasm and the nucleus, and the slow-diffusion-mobility (FAF curve *3* in Fig. 3) in the nucleus (summarized in Table 1). Fluorescent intensity at the point of slower diffusion was weak compared to that at other places in the nucleus. However, we could not specify the precise position of the slow-diffusion-mobility in the cell nucleus because of the very weak fluorescence in the nucleus. Fig. 3 *G* shows a plot superimposing normalized FAFs of $EGFP_n$ measured in the nucleus of HeLa cell excluding the slow-diffusion-mobility. The FAF of each oligomeric EGFP in the cell nucleus shifted to the right with the size of tandem $EGFP_n$. This shift was well consistent with the result in aqueous solution (Fig. 2 *A*). This consistency suggests that the fast-diffusion-mobility of oligomeric $EGFP_n$ in the cell nucleus might follow the diffusion model of a rod-like molecule.

Analysis of FAF in cells was performed with a two-component model ((Eq. 2), $i = 1$ and 2), a fast diffusing component (first component) and a slower diffusing

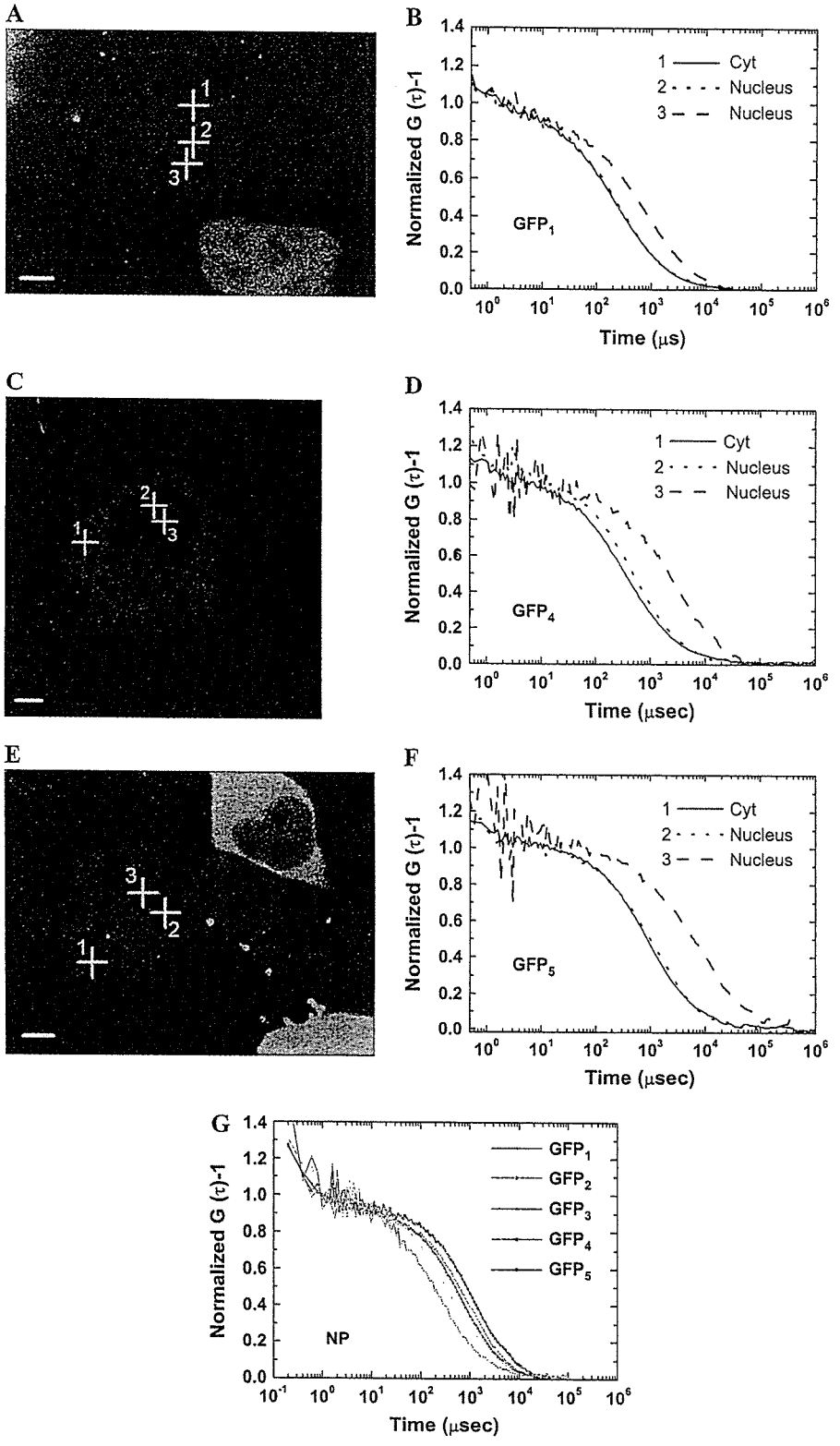

FIGURE 3 Two kinds of diffusional mobility in the nucleus. For FCS analysis, very weakly fluorescent and nonphotobleaching cells less than the molecular number of $N = 20$ in the detection volume of FCS, which corresponds to a concentration under 10^{-7} M, were selected at 24 h after transfection. After recording LSM images of selected (*A*) HEK, (*C*) COS7, and (*E*) HeLa cells, FCS measurements were performed on multiple places in the cytoplasm and in the nucleus. Bars, 5 μm. For clarification, only three typical and normalized FAFs of $EGFP_1$, $EGFP_4$, and $EGFP_5$ in the cytoplasm (*curve 1*) and the nucleus (*curves 2 and 3*) in HEK, COS7, and HeLa cells are shown in panels *B*, *D*, and *F*, respectively. The rightward shift of the FAF curve indicates the slow-diffusion-mobility. The nucleus has both fast diffusion (*curve 2*) and much slower diffusion (*curve 3*). The normalized FAFs of EGFP and tandem $EGFP_n$ in the nucleus of a HeLa cell with the fast-diffusion-mobility (*curve 2*) are summarized in panel *G*. The normalized FAFs of the fast-diffusion-mobility were gradually shifted to the right according their molecular size. (Cyt, cytoplasm).

component (second component), because FAF of each tandem $EGFP_n$ cannot be fitted by a one-component model, but best fitted by the two-component model. However, some FAFs were best fitted by a one-component model. In this case, we adopted the result of one-component analysis (supplementary Fig. S2). The first component was considered to be a freely diffusing component and the second component was assumed to be a slowly diffusing component (14,24,42). High density of the cellular solutes and some restricted mobility in a cellular microstructure may slow

TABLE 1 Diffusion constants of monomeric EGFP and tandem $EGFP_n$ in the cytoplasm, the nucleoplasm, and the nucleolus in three different living cells (23)

		Fast (fraction)		Slow (fraction)	Very slow (fraction)
*Fast-diffusion-mobility (Cyt and NP)		(>90%)		–	(<10%)
Slow-diffusion-mobility (NL)		(<80%)		(20%~100%)	–
		Cyt (fast/first components)		NP (fast/first components)	
†Cell line	Type of GFP	D ($\mu m^2 s^{-1}$)	Fraction (%)	D ($\mu m^2 s^{-1}$)	Fraction (%)
HeLa	GFP_1	23.4 ± 2.5	95	22.7 ± 2.3	96
	GFP_2	16.4 ± 0.8	92	14.9 ± 0.8	93
	GFP_3	13.1 ± 1.4	91	11.6 ± 1.7	91
	GFP_4	9.0 ± 0.8	93	8.6 ± 0.6	90
	GFP_5	8.3 ± 1.1	90	7.8 ± 1.2	90
COS7	GFP_1	27.1 ± 3.0	90	22.3 ± 1.3	95
	GFP_2	15.8 ± 1.0	93	14.9 ± 0.3	92
	GFP_3	14.7 ± 0.6	91	11.1 ± 0.8	94
	GFP_4	10.8 ± 1.0	92	9.2 ± 0.8	91
	GFP_5	9.5 ± 1.0	90	7.9 ± 0.4	90
HEK	GFP_1	21.0 ± 1.6	95	24.9 ± 2.1	93
	GFP_2	17.4 ± 3.5	92	16.4 ± 2.2	95
	GFP_3	14.1 ± 1.4	91	13.2 ± 0.9	91
	GFP_4	10.3 ± 1.1	90	10.5 ± 1.8	90
	GFP_5	10.4 ± 0.5	92	9.6 ± 0.4	92
		NL (fast/first components)		NL (slow/second components)	
Cell line	Type of GFP	$D^{\ddagger}$ ($\mu m^2 s^{-1}$)	Fraction (%)	$D^{\ddagger}$ ($\mu m^2 s^{-1}$)	Fraction (%)
HeLa	GFP_1	24.2 ± 1.3	–	5.8 ± 1.6	–
	GFP_2	17.6 ± 1.2	–	3.8 ± 0.5	–
	GFP_3	13.0 ± 1.0	–	2.1 ± 0.3	–
	GFP_4	11.0 ± 0.7	–	1.9 ± 0.1	–
	GFP_5	8.9 ± 0.4	–	1.6 ± 0.4	–
COS7	GFP_1	22.8 ± 1.7	–	5.7 ± 1.6	–
	GFP_2	16.1 ± 2.9	–	3.7 ± 0.8	–
	GFP_3	13.3 ± 1.5	–	1.7 ± 0.2	–
	GFP_4	9.0 ± 0.3	–	1.3 ± 0.2	–
	GFP_5	9.1 ± 0.8	–	1.1 ± 0.2	–

*Two kinds of mobility, fast-diffusion-mobility and slow-diffusion-mobility, were differentiated by two-component analysis of $G(\tau)$. The fast-diffusion-mobility has "fast" and "very slow" components. In contrast, the slow-diffusion-mobility has "fast" and "slow" components. These three components have different ranges for the diffusion time and fraction.

†The diffusion constants and fractions in cytoplasm (Cyt) and nucleoplasm (NP) correspond to the average diffusion constants and fractions for the first component of the fast-diffusion-mobility ("fast" in top part of table). The diffusion constant and fractions of the second component ("very slow" in top part of table) is not shown. The diffusion constant in the nucleolus (NL) corresponds to those for the first component ("fast" in top part of table) and the second component ("slow" in top part of table) of the slow-diffusion-mobility. The fraction in the NL was not shown because the values were very variable (see also the text). The values of D in NL indicated those having a fraction >50%. Data were averaged over 15–20 cells for HeLa, COS7, and HEK293 (Mean ± SE of three independent experiments).

‡The average values of D in the nucleolus were obtained from cells only expressing monomer EGFP and tandem EGFPn without mRFP-fibrillarin. These values were consistent with the result of Fig.5 *E* obtained by coexpressed cells.

down free diffusion. With conditions of cells having a concentration under 20 $EGFP_n$ molecules (<0.1 μM) and a comparatively short measurement time under 30 s, the influence of photobleaching on diffusion time, which gives rise to a very long diffusion time and an increase of the fraction (y_i value in Eq. 2), could be minimized. Photobleaching effects were checked from the time trace of fluorescent intensity for all FCS data (supplementary Fig. S3). Increasing the incubation time after transfection for a few days made the effect of photobleach on FCS measurement much stronger, because the promoter for protein expression is strong and not a controlled one. In practice, photobleaching effect was very small for weakly fluorescent cells at an early stage after expression of tandem GFP (supplementary Fig. S4). Background fluorescent signals under 2×10^3 cps and 10×10^3 cps were detected in medium and nontransfected HeLa, HEK, and COS7 cells (14). No significant correlation amplitudes were detected in the culture medium. In contrast, very weak correlations with very long diffusion times above 10^5 μs were sometimes detected in each cell type when FCS measurement was carried out over longer duration over 60 s. This was derived from very slow

and large fluctuation of fluorescence but not from photobleaching. To solve the background with very slow fluctuation, we adapted a shorter measurement time as described above. Considering each tandem EGFP has much larger brightness per molecule than that of monomer EGFP (C. Pack and M. Kinjo, unpublished data) and the diffusion time of the proteins was an order of millisecond ranges, the short measurement time of FCS might be enough to obtain a reliable autocorrelation function.

Two diffusional mobility in the nucleus

The fast-diffusion-mobility in the cytoplasm and the nucleus

Fig. 4 *A* shows a plot of the diffusion time of first component obtained from FAFs representing the fast-diffusion-mobility in the cytoplasm and in the nucleus of HeLa cells (curves *1* and *2* in Fig. 3, *B*, *D*, and *F*). For these FAFs of the fast-diffusion-mobility, >90% of the fraction (y_1 in Eq. 2) was defined as the first component, which represents free diffusion. These results were highly reproducible. As shown in Fig. 4 *A* (*solid circles*), the diffusion times of the fast-diffusion-mobility in the nucleus were gradually increased with the increase in the molecular size of tandem $EGFP_n$. In the cytoplasm (Fig. 4 *A*, *open circles*), the diffusion time of the first component for $EGFP_n$ also increased with size. No significant difference between the first components in the cytoplasm and nucleus was found. Average diffusion times of monomeric and oligomeric EGFP in HEK and COS7 cells also increased with increasing the size both in the cytoplasm and in the nucleus (Fig. 4, *B* and *C*). The ratio of the diffusion time of the first component in the cytoplasm and the nucleus of each cell type to that in aqueous solution ($DT_{cell}/DT_{sol.}$), which indicates the ratio of viscosity (Eqs. 3 and 4), is shown in inserts in Fig. 4, *A*, *B* and *C*, respectively. Regardless of the cell type, the average ratios of viscosities in the cytoplasm and the nucleus were not significantly different and 3.5-fold higher than that in solution. Moreover, there was no dependency of the viscosity ratio on the size of oligomeric $EGFP_n$. These results agreed with previous results obtained from microinjected fluorescent macromoleucules and monomeric EGFP (7,13,42).

Using the result that the average viscosity in the cytoplasm and nucleus was 3.5-fold higher than that in solution, the expected diffusion times of tandem $EGFP_n$ in the cell were calculated. As shown in Fig. 2, the measured diffusion times of first components in living cells were also compared with three calculated diffusion times (Fig. 4, *A*, *B*, and *C*) assuming the shape of oligomeric EGFP to be spherical (*dashed lines*) or rod-like with the expected linker lengths of 4 nm (*solid lines*) and 9 nm (*dotted lines*). Dependency of the diffusion times on the size of oligomeric EGFP both in the cytoplasm and in the nucleus was consistent with that of a rod-like molecule rather than a spherical one (*dashed lines*). Based on the result that the diffusion properties of rod-like molecules of oligomeric EGFP in the cytoplasm and the nucleus are equivalent and consistent with the result in aqueous solution, the oligomeric $EGFP_n$ located in the nucleus was not truncated or degraded. Consequently, our results suggested that the diffusion of oligomeric $EGFP_n$ as a rod-like molecule was well conserved in the cellular circumstance in all of three cell lines.

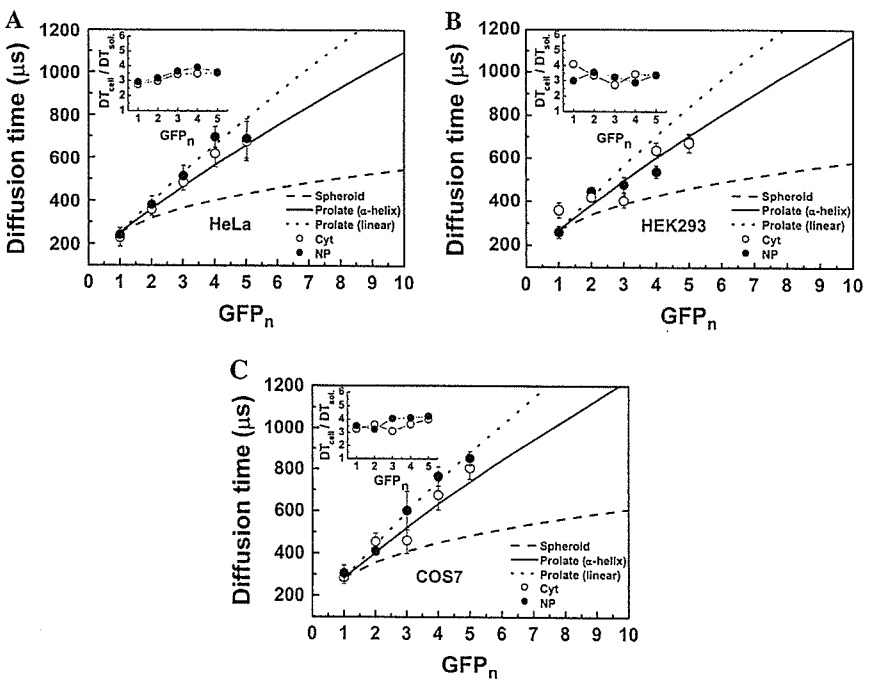

FIGURE 4 Fast diffusional mobility of tandem $EGFP_n$ is dependent on the molecular length. FAFs were fitted with a two-component model using Eq. 2, $i = 2$ for analyzing the diffusion times and the fractions of components 1 and 2. For the FAFs of the fast-diffusion-mobility in Fig. 3 *G*, the fraction of the first component was >90% for EGFP and tandem $EGFP_n$ in the cytoplasm and the nucleus. The diffusion times of the first components in HeLa cells (*A*), HEK cells (*B*), and COS7 cells (*C*) are plotted. The plots of measured diffusion times shown in panels *A*, *B*, and *C* show the average values of five cells for each protein. The error bars represent mean ± SD. The diffusion times of the first components were increased according to the molecular weight. As shown in Fig. 2, the calculated diffusion times for a spherical and a rod-like molecule were plotted for comparison. Dashed line shows diffusion times calculated by Eq. 5 using the molecular weight and the measured diffusion time of Rh6G assuming the oligomeric $EGFP_n$ are spherical. Solid and dotted lines show the calculated diffusion times assuming that the linker between EGFP forms a rigid α-helix and a linear shape, respectively. Inserts show the ratio of diffusion times of the first component in the cytoplasm and the nucleus to that in aqueous solution.